# Critical differences in 3D atomic structure of individual ligand-protected nanocrystals in solution

**Authors:** Byung Hyo Kim[1,2,†], Junyoung Heo[1,2,†], Sungin Kim[1,2], Cyril F. Reboul[3,4], Hoje Chun[5], Dohun Kang[1,2], Hyeonhu Bae[6], Hyejeong Hyun[7], Jongwoo Lim[7], Hoonkyung Lee[6], Byungchan Han[5], Taeghwan Hyeon[1,2], A. Paul Alivisatos[8,9,10], Peter Ercius*[,11], Hans Elmlund*[,3,4], Jungwon Park*[,1, 2]

**Affiliations:**

[1] Center for Nanoparticle Research, Institute for Basic Science (IBS), Seoul 08826, South Korea.

[2] School of Chemical and Biological Engineering, Institute of Chemical Process, Seoul National University, Seoul 08826, South Korea.

[3] Department of Biochemistry and Molecular Biology, Biomedicine Discovery Institute, Monash University, Clayton, VIC 3800, Australia.

[4] ARC Centre of Excellence for Advanced Molecular Imaging, Clayton, VIC 3800, Australia.

[5] Department of Chemical and Biomolecular Engineering, Yonsei University, Seoul 03722, South Korea.

[6] Department of Physics, Konkuk University, Seoul 05029, South Korea.

[7] Department of Chemistry, Seoul National University, Seoul 08826, South Korea.

[8] Department of Chemistry, University of California, Berkeley, CA 94720, USA.

[9] Material Sciences Division, Lawrence Berkeley National Laboratory, Berkeley, CA 94720, USA.

[10] Kavli Energy NanoScience Institute, Berkeley, CA 94720, USA.

[11] National Center for Electron Microscopy, Molecular Foundry, Lawrence Berkeley National Laboratory, Berkeley, CA 94720 USA.

*Correspondence to: percius@lbl.gov, hans.elmlund@monosh.edu, or jungwonpark@snu.ac.kr.

†These authors contributed equally to this work.

**Abstract:** Precise 3D atomic structure determination of individual nanocrystals is a prerequisite for understanding and predicting their physical properties. Nanocrystals from the same synthesis batch display what are often presumed to be small but possibly important differences in size, lattice distortions, and defects which can only be understood by structural characterization with high spatial 3D resolution. We solve the structures of individual colloidal Pt nanocrystals by developing atomic-resolution 3D liquid-cell electron microscopy to reveal critical intrinsic heterogeneity of ligand-protected Pt nanocrystals in solution, including structural degeneracies, lattice parameter deviations, internal defects, and strain. These differences in structure lead to significant contributions to free energies, consequential enough that they must be considered in any discussion of fundamental nanocrystal properties or applications.

**One Sentence Summary:** 3D liquid cell TEM reveals critical differences in the atomic structures of individual colloidal Pt nanocrystals.

**Main Text:**

The three dimensional (3D) atomic arrangement of materials determines their physical and catalytic properties (*1, 2*). The 3D structures of nanocrystals typically deviate from the periodic atomic arrangement of their bulk counterparts due to the dominance of surface dangling bonds, defects, dislocations, as well as intrinsic quantum effects due to finite size (*3-5*). Such deviations are more pronounced in small nanocrystals of less than 4 nm in diameter. For example, interatomic distances near the surface of Au nanocrystals are shortened compared to the perfect face-centered cubic (fcc) structure of bulk Au (*6*), whereas cerium oxide nanocrystals show extended interatomic distances near the surface (*7*). Au nanoparticles below a critical size can have an icosahedral structure that is thermodynamically unfavored in the bulk counterpart (*8*). These unique physical properties make nanocrystals attractive as heterogeneous catalysts (*9*). Populations of synthesized nanocrystals tend to have heterogeneous atomic structures, since uniform control at the level of individual nanocrystals is extremely difficult to accomplish (*10, 11*). The organic ligands and solvents used in a typical colloidal synthesis coordinate surface atoms and further affect the crystal and electronic structures of nanocrystals (*12-16*). Thus, understanding their unique properties requires precise and reproducible determination of the positions of the individual atoms at the level of a single nanocrystal directly from the solution phase, in which most of catalytic and chemical reactions occur.

The 3D atomic structures of nanocrystals can be determined by electron tomography whereby the structures are reconstructed from a tilt series of transmission electron microscopy (TEM) images (*17-20*). However, this method relies on image acquisition under vacuum and on a substrate, which can cause structural deformation of the nanocrystals. Furthermore, the spatial resolution is frequently non-uniform in 3D space due to missing projection directions (*21*). Single-particle reconstruction based on cryo-TEM, as an alternative approach, is also not appropriate for studying heterogeneous nanocrystal populations, since the analysis relies on 2D images collected from a large number of different particles assumed to have the same structure (*22*). We previously introduced 3D SINGLE (Structure Identification of Nanoparticles by Graphene Liquid cell Electron microscopy) as a direct method to resolve 3D structures of nanocrystals in solution, but the resolution obtained was only sufficient to determine overall morphologies in 3D (*23*), and the understanding of how to analyze such information in order to extract key structure factors was still limited.

We develop a "Brownian one-particle reconstruction" method—atomic-resolution 3D SINGLE—and apply it to analyze the 3D atomic arrangements of individual Pt nanocrystals in solution. Our high-resolution 3D density maps of eight individual Pt nanocrystals from the same synthesis batch and fitted atomic models show fcc structures with structural heterogeneity, including single crystalline, distorted structures, and a dislocation. The precise assignment (+/- 19 pm) of the 3D atomic positions allowed direct investigation of lattice expansion, internal defects, strain near the surfaces and dislocation planes, and their contribution to the free energy. The resulting information shows that structural information obtained in a realistic solution based on the SINGLE method can provide a vital new guide for future improved synthesis and for understanding the properties of the current materials.

**3D reconstruction from electron microscopy images of Pt nanocrystals in liquid**

Atomic-resolution 3D SINGLE of nanocrystals in solution was achieved through aberration corrected TEM imaging, using a direct electron detector with high temporal (2.5 msec) resolution (fig. S1). The high temporal resolution allowed us to capture projection images of the nanocrystals in different views as they were tumbling in solution. The individual particles were tracked throughout the time-series and the extracted trajectory of 2D images were reconstructed to obtain Coulomb charge 3D density maps of the individual particles (see supplementary materials and movie S1). Obtaining thousands of high-resolution images within a few seconds allowed complete coverage of the projection angles, which is required for accurate 3D reconstruction. The 3D orientations of the projections of the randomly rotating nanocrystals were determined using an iterative Fourier 3D reconstruction algorithm based on stochastic hill climbing (*24*). In order to overcome uncertainties originating from the random movement and innate noise in the TEM images, we developed algorithms for motion correction and subtraction of the background introduced by the liquid cell (see supplementary materials). These are key steps in the advanced 3D reconstruction algorithm to obtain high-resolution 3D density maps.

Representative Pt nanocrystal density maps are depicted in Fig. 1A and movie S2. The reconstructed 3D density maps of the nanocrystals have resolutions better than 0.72 Å according to the 0.143 Fourier shell correlation (FSC) criterion (fig. S2) (*25*), allowing assignment of the positions of all constituent atoms in 3D space within the domain of each nanocrystal (Fig. 1B and figs. S3 to S5). The assigned atomic coordinates can further be used to calculate the formation energy of individual nanocrystals (table S1). We obtained strain maps from the atomic position information, which indicate the lattice distortion (Fig. 1C and fig. S6). Sliced 3D maps provide detailed structural information and strain tensors (an example for one Pt nanocrystal is shown in Fig. 1D).

The reconstruction method and the resulting 3D maps were validated in several ways (see supplementary materials). First, the algorithm was verified by reconstructing multi-slice simulated TEM images of model fcc nanocrystals with 2.5 nm and 4.0 nm diameter with varying parameters including different pixel resolutions and binning process to mimic the imaging mechanism in TEM (figs. S7 to S9) (*26*). To confirm the robustness of the reconstruction method with significant random noise that originates from TEM imaging of liquid, multi-slice simulated TEM images including model nanocrystals and water molecules that continuously change orientation and geometry are generated by using molecular dynamics (MD) simulation and used for successful verification of 3D reconstruction (supplementary materials and figs. S10 and S11). Second, to validate the experimental 3D structures, we confirmed that re-projected images of the obtained 3D electron density maps were in good agreement with the original projections (fig. S12 and S13). Third, we repeated the reconstruction process by using simulated images obtained by multi-slice simulation of the atomic position map and measured the similarity between the 3D atomic structures from the original TEM images and the simulated images (fig. S14). The average root mean square difference is 9.9 pm to 19 pm (fig. S14). In addition, the projection directions of the rotating nanocrystals show wide coverage (fig. S15), indicating that the 3D maps include ample crystallographic information obtained from numerous zone axes. Experiments on simulated data show that vertical movement of the nanocrystals has a negligible effect on the final atomic structure (fig. S16).

**Effects of surface ligands on the 3D atomic structures of Pt nanocrystals**

The Pt nanocrystals were prepared by a typical optimized synthesis to make the final population homogeneous in terms of size and shape distribution, but it is widely known that the individual crystal structures do not have identical atomic arrangements due to the complexity of their growth trajectories (*27*). Our reconstructed 3D density maps (Fig. 1A and fig. S3A) and corresponding atomic coordinate maps (Fig. 1B and fig. S3B) show this expected structural heterogeneity. Many of the nanocrystals from the same synthesis batch are single crystalline with fcc atomic arrangements, with the exception of heterogeneity due to slight variation in diameter of 2.25, 2.41, 2.42, 2.52, 2.66, and 2.92 nm for Particle 1 to 6, respectively, as shown in Fig. 1. Some of the nanocrystals incorporate more diversity in their structures. Shear distortions (Particle 7 in Fig. 1) and dislocations (Particle 8 in Fig. 1) are frequently observed in the reconstructed 3D density and atomic position maps.

Our 3D density and atomic position maps match the expected fcc atomic structure. Projections along the [100] zone axis of the 2.52 nm-sized nanocrystal (Particle 4) show that the atoms are positioned with 4-fold symmetry at a lattice spacing of 2.0 Å, which corresponds to the Pt (200) plane distance (Fig. 2A). A 45-degree rotation around [001] (Fig. 2A) reveals a typical lattice projection along the [110] axis with lattice spacing of two 2.2 Å (111) and one 2.0 Å (200) (Fig. 2B). In addition, in a view along the [111] zone axis, the 3D structure exhibits the hexagonal close packing arrays of atoms (Fig. 2C). The fcc structure can also be identified by an ABC packing sequence along the [111] direction, where every third layer is in the same position (Fig. 2D). Due to this close packing structure, the nanocrystals have a coordination number of 12 with the exception of surface atoms (fig. S17).

As nanocrystals become smaller, the fraction of surface atoms becomes significant. Having dangling bonds with surface organic ligands, differently from the perfect symmetric coordination in a bulk crystal, surface atoms contribute asymmetric atomic orbital overlaps with inner atoms (*28*). In addition, the electronic structure of small nanocrystals can be remarkably affected by atomic defects (*29*). To understand microscopic structural details of nanocrystals and the extent that the bulk crystal motif is maintained at the nanoscale, we measured all interatomic distances along the <111>, <100>, and <110> directions (see the supplementary materials) and plotted them according to the distance from the center (Fig. 2E). While the interatomic distances are almost constant near the core, they deviate gradually toward the surface, indicating noticeable deviation of surface atoms from their periodic positions.

By fitting the atomic coordinates, we found an overall expansion of the fcc lattice structure. For example, the lattice parameters of Particle 4 are a=3.990 Å, b=3.985 Å, c= 3.990 Å, α=89.96°, β=89.70°, and γ=89.75°. Interestingly, such lattice expansion is consistently observed in other nanoparticles (*30, 31*). The averaged fcc unit cell lattice constants of the 2.25, 2.41, 2.42, 2.52, 2.66 and 2.92 nm-sized nanocrystals are 3.96, 4.02, 4.00, 3.99, 3.96, and 3.97 Å, respectively, which are 1.02, 2.56, 2.02, 1.74, 0.95 and 1.22% larger than the bulk values, respectively (Fig. 3A). The lattice expansion can be effectively described by the radial strain ($\varepsilon_{rr}$), which is defined as $\epsilon_{rr} = \frac{\partial u_r}{\partial r}$, where $r$ is the distance between an atom and the center of mass of a particle and $u_r$ is radial displacement (fig. S18). Consistent with our observed deviations of lattice parameters, the arithmetic mean (averaged over all atom positions) radial strain is positive for Particle 1 through 6 (Fig. 3B). We re-visited previous X-ray diffraction (XRD) studies of ligand-protected nanocrystals and found that such lattice expansion, which was unrecognized because the peak shift was very small, is observed consistently in PVP-protected metal nanocrystals (*30, 31*). We also checked our PVP-protected Pt nanocrystals using synchrotron XRD experiments. XRD patterns

exhibit a slightly enlarged lattice parameter (3.976 Å) compared to that of bulk Pt (Fig. 3C). These observations imply that crystal structures of Pt nanocrystals tend to expand slightly when protected by polyvinylpyrrolidone (PVP) surface ligands in the native solution phase. These results are in contrast to lattice compressions theoretically observed for metal nanocrystals without protecting ligands, which is explained by the effect of surface tension and strong bonding of surface atoms with low coordination numbers (*6*). Our results indicate that such effects can be weakened and even reversed when surface ligands are adsorbed on the metal nanocrystals in the solution phase. We performed density functional theory (DFT) calculations, and showed that the adsorption of PVP ligands can induce localization of electron density around surface Pt atoms. As a result, the inward metallic bonds are weakened while increasing the atomic distance (Fig. 3, E and F). Since the PVP ligands are long polymers decorated with multiple binding functional groups, the coverage of polymeric binding may not be uniform across the surface. This is likely to induce local deviation of the atomic lattice and the resulting surface strain. Particular surface regions of a Pt nanocrystal, where binding of pyrrolidone groups are more dominant, are presumably expanded. Our radial strain measurements show such a localization on specific surface regions of the particle (see Fig. 3G).

The observed lattice fluctuations and the expansion of the fcc crystal structure are difficult to measure in conventional high-resolution TEM images of nanocrystals, since the interatomic distances are averaged over each atomic column along the projection direction. Further, motion in the liquid makes it difficult to capture the correct zone axis with the high precision required. Our atomic-resolution 3D SINGLE method overcomes these limitations and allows measurement of the interatomic distances between all constituent atoms in 3D space, enabling detailed structural characterization. We confirmed that the lattice fluctuations are not due to inaccuracy of the reconstruction method. Accurate interatomic distances were measured in the 3D atomic position map generated from reconstructing simulated noisy TEM images of a model nanocrystal with a perfect fcc structure. They consistently follow bulk fcc parameters with a very marginal deviation throughout the volume of the nanocrystal (fig. S7C). Thus, the observed deviation of the lattice parameter is inherent to these small ligand-protected Pt nanocrystals.

Using the experimentally determined atomic positions, the formation energy of each nanocrystal can be directly evaluated using DFT calculation without relaxation processes. Overall, the higher strained particles require a higher formation energy as shown in Fig. 3D. (see supplementary materials) Highly-strained nanocrystals, such as distorted particles, show high formation energies attributed to the strain field (Fig. 3D). It is possible that the energetically metastable structures, including the dislocations, are kinetically trapped during complicated synthetic reactions that incorporate particle coalescence (*23*). The DFT calculation considered bare surfaces for reliable comparison between nanocrystals without uncertainty originating from the complexity of ligand passivation (table S1). Considering the stabilization effect of surface binding groups, the formation energy of nanocrystals with PVP ligands can be substantially reduced (fig. S19, table S2).

**Structural heterogeneity of Pt nanocrystals**

Our 3D density and atomic position maps reveal that Pt nanocrystals have more complicated crystal structures than the single crystalline fcc structure. The atomic arrangement of the distorted nanocrystal (Particle 7) is slightly bent around a (110) plane (Fig. 4, A to C). Overlaying different

atomic planes from each domain as red and blue reveal that the lattice points of the two domains are slightly mismatched (Fig. 4C). In addition, several vacancies are observed near the boundary (Fig. 4B).

Particle 8 has a $(1\bar{1}1)$ partial edge dislocation, as viewed along a [121] zone axis in Fig. 4D. This is a Shockley partial dislocation with the Burger's vector of a/2<111> and a gliding plane of $(10\bar{1})$. The atoms near the dislocation are highly disordered (Fig. 4E) while other atoms conform to an fcc lattice. A magnified image of a $(1\bar{1}1)$ plane (Fig. 4F), which is perpendicular to the gliding plane, shows a hexagonal array within each domain and breakage of periodicity near the boundary between the two domains. The origin of the disordered structure of the nanocrystal can be explained by coalescence events during the formation of the nanocrystals (*23*, *32*). Recent liquid phase TEM studies have revealed that Pt nanocrystals frequently coalesce along low index surfaces and become multi-domain structures when they grow by an aggregative pathway (*23*, *27, 33, 34*).

**Strain analysis of individual Pt nanocrystals from the 3D atomic maps**

Strain imposed on the constituent atoms determines catalytic activities of metal nanocrystals because the strain modifies the local binding energy with adsorbates by changing the band width of *d* orbitals (*35*). Engineering tensile strain is indeed successfully applied in tuning reactivity of Pt nanocrystals in many important catalytic reactions including the methanol oxidation reaction (*36*) and the oxygen reduction reaction (*37*). Strain analysis at high resolution will be an important asset in understanding catalytic performance of heterogeneous catalysts and tuning their performance. Using the fcc structure with a bestfit lattice parameter as a reference, we obtained 3D strain maps by calculating the atomic displacement field, convolving it with 2 Å-wide 3D Gaussian kernel, and differentiating it (Fig. 5, figs. S20 and S21) (*17*). We also used geometric phase analysis (GPA) (*38*) for comparison. Both methods showed similar results (fig. S22). The full 6-element strain tensor of Particle 4 is mapped for each atomic position in 3D space (Fig. 5A). The strain maps clearly show that the surface of the nanocrystals has larger strain compared to the core atoms (Figs. 1D and 5B). The strain distributions of the surface atoms, defined as $r > R - d_{111}$, where $r$ is the distance of an atom from the center of mass, $R$ is the radius of the nanocrystal, and $d_{111}$ is the bulk Pt(111) plane distance, are 1.89, 2.27, 1.92, 1.54, 1.49, and 1.52%, while those of core atoms are 1.14, 1.28, 1.15, 1.07, 0.66, and 0.93% for $\varepsilon_{xx}$, $\varepsilon_{yy}$, $\varepsilon_{zz}$, $\varepsilon_{xy}$, $\varepsilon_{yz}$, and $\varepsilon_{zx}$, respectively (Fig. 5B and fig. S23). The broader strain distribution of the surface atoms is due to the disorder of the surface atoms, presumed to be accommodated by surface ligand protection. Tensile strain occurs throughout the nanocrystal for both surface and core atoms. The average strains of $\varepsilon_{xx}$, $\varepsilon_{yy}$, and $\varepsilon_{zz}$ (parallel to the <100> directions) for Particle 4 are 1.54, 1.49, and 1.58%, respectively, consistent with the expanded lattice parameters obtained by fitting of the atomic coordinates.

The distorted Pt nanocrystal (Particle 7) also shows tensile strain throughout the nanocrystal and large strain distribution on the surface. Due to its structural deformation, the strain distribution of the distorted particle is 2.23 %, which is 1.7 times broader than that of the single crystal (Particle 4; 1.31%). In addition, the bent structure leads to high shear strain of atoms at the domain boundary (Fig. 5C), resulting in a bimodal shear strain distribution with two distribution centers (Fig. 5D). The nanocrystal with the dislocation also shows large strains at the domain boundary (Particle 8 in Fig. 1C), which is known to enhance catalytic activities (*39*).

## Conclusion

We show that high-resolution 3D atomic arrangements of Pt nanocrystals synthesized from a single batch have critical structural differences. This was made possible by the development of atomic-resolution 3D SINGLE for solving the structure of nanocrystals in solution phase. Our results can be understood by the nature of typical colloidal synthesis of nanocrystals which thermodynamically deviates from expectations based on bulk crystallography. Structure and strain analysis enabled by assignment of precise atomic positions reveals lattice expansions of ligand-protected metal nanocrystals in solution and the existence of large strain near domain boundaries, dislocation edges, and surfaces. The detailed structural information we introduce is strongly linked to the origin of the catalytic performance of Pt nanocrystals. We also demonstrate that the precise atomic structures obtained by our approach can be utilized in computational chemistry to improve the accuracy of property predictions of nanocrystals. Atomic-resolution 3D SINGLE can apply to nanocrystals with various composition (fig. S24) and atomic structural integrity. It will find applications in other systems, including colloidal nanomaterials and biological macromolecules, where structural information in solution is required.

## References and Notes:

1. M. A. Pfeifer, G. J. Williams, I. A. Vartanyants, R. Harder, I. K. Robinson, Three-dimensional mapping of a deformation field inside a nanocrystal. *Nature* **442**, 63 (2006).
2. M. Cargnello, V. V. T. Doan-Nguyen, T. R. Gordon, R. E. Diaz, E. A. Stach, R. J. Gorte, P. Fornasiero, C. B. Murray, Control of metal nanocrystal size reveals metal-support interface role for ceria catalysts. *Science* **341,** 771-773 (2013).
3. L. Hultman, S. Stafström, Z. Czigány, J. Neidhardt, N. Hellgren, I. F. Brunell, K. Suenaga, C. Colliex, C-linked nano-onions of carbon nitride in the solid phase: Existence of a novel $C_{48}N_{12}$ aza-fullerene. *Phys. Rev. Lett.* **87,** 225503 (2001).
4. M. Azubel, J. Koivisto, S. Malola, D. Bushnell, G. L. Hura, A, L. Koh, H. Tsunoyama, T. Tsukuda, M. Pettersson, H. Häkkinen, R. D. Kornberg, Electron microscopy of gold nanoparticles at atomic resolution. *Science* **345,** 909-912 (2014).
5. T. Nilsson Pingel, M. Jørgensen, A. B. Yankovich, H. Grönbeck, E. Olsson, Influence of atomic site-specific strain on catalytic activity of supported nanoparticles. *Nat. Commun.* **9**, 2722 (2018).
6. Z. Huang, P. Thomson, S. Di, Lattice contractions of a nanoparticle due to the surface tension: A model of elasticity. *J. Phys. Chem. Solids* **68**, 530-535 (2007).
7. L. Chen, P. Fleming, V. Morris, J. D. Holmes, M. A. Morris, Size-related lattice parameter changes and surface defects in ceria nanocrystals. *J. Phys. Chem. C* **114**, 12909–12919 (2010).
8. Y. Negishi, T. Nakazaki, S. Malola, S. Takano, Y. Niihori, W. Kurashige, S. Yamazoe, T. Tsukuda, H. Häkkinen, A critical size for emergence of nonbulk electronic and geometric structures in dodecanethiolate-protected Au clusters. *J. Am. Chem. Soc.* **137**, 1206–1212 (2015).
9. W. Zhu, Y.-J. Zhang, H. Zhang, H. Lv, Q. Li, R. Michalsky, A. A. Peterson, S. Sun, active and selective conversion of $CO_2$ to CO on ultrathin Au nanowires. *J. Am. Chem. Soc.* **136**, 16132–16135 (2014).

10. S. G. Kwon, T. Hyeon, Formation mechanisms of uniform nanocrystals via hot-injection and heat-up methods. *Small* **7**, 2685–702 (2011).
11. W. Gao, P. Tieu, C. Addiego, Y. Ma, J. Wu, X. Pan, Probing the dynamics of nanoparticle formation from a precursor at atomic resolution. *Sci. Adv.* **5**, eaau9590 (2019).
12. Z. Fan, X. Huang, Y. Han, M. Bosman, Q. Wang, Y. Zhu, Q. Liu, B. Li, Z. Zeng, J. Wu, W. Shi, S. Li, C. L. Gan, H. Zhang, Surface modification-induced phase transformation of hexagonal close-packed gold square sheets. *Nat. Commun.* **6**, 6571 (2015).
13. K. Yang, X. Chen, Z. Zheng, J. Wan, M. Feng, Y. Yu, Solvent-induced surface disorder and doping-induced lattice distortion in anatase $TiO_2$ nanocrystals for enhanced photoreversible color switching. *J. Nanoparticle Res.* **20**, 255 (2018).
14. W. Wu, E. V. Shevchenko, The surface science of nanoparticles for catalysis: electronic and steric effects of organic ligands. *J. Mater. Chem. A* **7**, 3863–3873 (2019).
15. F. Bertolotti, D. N. Dirin, M. Ibáñez, F. Krumeich, A. Cervellino, R. Frison, O. Voznyy, E. H. Sargent, M. V. Kovalenko, A. Guagliardi, N. Masciocchi, Crystal symmetry breaking and vacancies in colloidal lead chalcogenide quantum dots. *Nat. Mater.* **15,** 987–994 (2016).
16. T. Altantzis, I. Lobato, A. De Backer, A. Béché, Y. Zhang, S. Basak, M. Porcu, Q. Xu, A. Sánchez-Iglesias, L. M. Liz-Marzán, G. Van Tendeloo, S. Van Aert, S. Bals, Three-dimensional quantification of the facet evolution of Pt nanoparticles in a variable gaseous environment. *Nano Lett.* **19,** 477-481 (2019).
17. R. Xu, C.-C. Chen, Li Wu, M. C. Scott, W. Theis, C. Ophus, M. Bartels, Y. Yang, H. Ramezani-Dakhel, M. R. Sawaya, H. Heinz, L. D. Marks, P. Ercius, J. Miao, Three-dimensional coordinates of individual atoms in materials revealed by electron tomography. *Nat. Mater.* **14**, 1099-1103 (2015).
18. Y. Yang, C.-C. Chen, M. C. Scott, C. Ophus, R. Xu, A. Pryor, L. Wu, F. Sun, W. Theis, J. Zhou, M. Eisenbach, P. R. C. Kent, R. F. Sabirianov, H. Zeng, P. Ercius, J. Miao, Deciphering chemical order/disorder and material properties at the single-atom level. *Nature* **542**, 75-79 (2017).
19. B. Goris, S. Bals, W. Van den Broek, E. Carbó-Argibay, S. Gómez-Graña, L. M. Liz-Marzán, G. Van Tendeloo, Atomic-scale determination of surface facets in gold nanorods. *Nat. Mater.* **11**, 930-935 (2012).
20. J. Miao, P. Ercius, S. J. L. Billinge, Atomic electron tomography: 3D structures without crystals. *Science* **353,** aaf2157 (2016).
21. A. Bartesaghi, P. Sprechmann, J. Liu, G. Randall, G. Sapiro, S. Subramaniam. Classification and 3D averaging with missing wedge correction in biological electron tomography. *J. Struct. Biol.* **162**, 436–450 (2008).
22. Y. Cheng, Single-particle cryo-EM at crystallographic resolution. *Cell* **161**, 450–457 (2015).
23. J. Park, H Elmlund, P. Ercius, J. M. Yuk, D. T. Limmer, Q. Chen, K. Kim, S. H. Han, D. A. Weitz, A. Zettl, A. P. Alivisatos, 3D structure of individual nanocrystals in solution by electron microscopy. *Science* **349,** 290-295 (2015).
24. C. F. Reboul, M. Eager, D. Elmlund, H. Elmlund, Single-particle cryo-EM—Improved ab initio 3D reconstruction with SIMPLE/PRIME. *Protein Sci.* **27**, 51–61 (2017).
25. M. van Heel, M. Schatz, Fourier shell correlation threshold criteria. *J. Struct. Biol.* **151**, 250–262 (2005).

26. E. J. Kirkland, *Advanced computing in electron microscopy* (Springer Science & Business Media, 2010).
27. J. M. Yuk, J. Park, P. Ercius, K. Kim, D. J. Hellebusch, M. F. Crommie, J. Y. Lee, A. Zettl, A. P. Alivisatos, High-resolution EM of colloidal nanocrystal growth using graphene liquid cells. *Science* **336,** 61-64 (2012).
28. S. Baumann, W. Paul, T. Choi, C. P. Lutz, A. Ardavan, A. J. Heinrich, Electron paramagnetic resonance of individual atoms on a surface. *Science* **350,** 417-420 (2015).
29. A. D. P. Leach, X. Shen, A. Faust, M. C. Cleveland, A. D. La Croix, U. Banin, S. T. Pantelides, J. E. Macdonald, Defect luminescence from wurtzite $CuInS_2$ nanocrystals: Combined experimental and theoretical analysis. *J. Phys. Chem. C* **120**, 5207–5212 (2016).
30. T. Teranishi, M. Hosoe, T. Tanaka, M. Miyake, Size control of monodispersed Pt nanoparticles and their 2D organization by electrophoretic deposition. *J. Phys. Chem. B* **103**, 3818–3827 (1999).
31. C. Song, O. Sakata, L. S. R. Kumara, S. Kohara, A. Yang, K. Kusada, H. Kobayashi, H. Kitagawa, Size dependence of structural parameters in fcc and hcp Ru nanoparticles, revealed by Rietveld refinement analysis of high-energy X-ray diffraction data. *Sci. Rep.* **6**, 31400 (2016).
32. J. C. Ondry, M. R. Hauwiller, A. P. Alivisatos, Dynamics and removal pathway of edge dislocations in imperfectly attached PbTe nanocrystal pairs: Toward design rules for oriented attachment. *ACS Nano* **12**, 3178–3189 (2018).
33. D. Li, M. H. Nielsen, J. R. I. Lee, C. Frandsen, J. F. Banfield, J. J. De Yoreo, Direction-specific interactions control crystal growth by oriented attachment. *Science* **336,** 1014-1017 (2012).
34. B. Luo, J. W. Smith, Z. Wu, J. Kim, Z. Ou, Q. Chen, Polymerization-like co-assembly of silver nanoplates and patchy spheres. *ACS Nano* **11**, 7626–7633 (2017).
35. M. Mavrikakis, B. Hammer, J. K. Nørskov, Effect of strain on the reactivity of metal surfaces. *Phys. Rev. Lett.* **81**, 2819–2822 (1998).
36. P. Strasser, S. Koh, T. Anniyev, J. Greeley, K. More, C. Yu, Z. Liu, S. Kaya, D. Nordlund, H. Ogasawara, M. F. Toney, A. Nilsson, Lattice-strain control of the activity in dealloyed core–shell fuel cell catalysts. *Nat. Chem.* **2**, 454 (2010).
37. X. Huang, Z. Zhao, L. Cao, Y. Chen, E. Zhu, Z. Lin, M. Li, A. Yan, A. Zettl, Y. M. Wang, X. Duan, T. Mueller, Y. Huang, High-performance transition metal–doped $Pt_3Ni$ octahedra for oxygen reduction reaction. *Science* **348,** 1230-1234 (2015).
38. M. J. Hÿtch, E. Snoeck, R. Kilaas, Quantitative measurement of disp lacement and strain fields from HREM micrographs. *Ultramicroscopy* **74**, 131–146 (1998).
39. R. G. Mariano, K. McKelvey, H. S. White, M. W. Kanan, Selective increase in $CO_2$ electroreduction activity at grain-boundary surface terminations. *Science* **358,** 1187-1192 (2017).
40. C. J. Kliewer, C. Aliaga, M. Bieri, W. Huang, C.-K. Tsung, J. B. Wood, K. Komvopoulos, G. A. Somorjai, Furan hydrogenation over Pt(111) and Pt(100) single-crystal surfaces and Pt nanoparticles from 1 to 7 nm: A kinetic and sum frequency generation vibrational spectroscopy study. *J. Am. Chem. Soc.* **132,** 13088-13095 (2010).
41. R. Kohavi, A study of cross-validation and bootstrap for accuracy estimation and model selection. in Proceedings of the 14th international joint conference on artificial intelligence 1137–1143 (Morgan Kaufmann Publishers Inc., 1995)

42. S. Grimme, Semiempirical GGA-type density functional constructed with a long-range dispersion correction. *J. Comput. Chem.* **27,** 1787−1799 (2006).

**Acknowledgments:** The experiments performed at the Molecular Foundry, Lawrence Berkeley National Laboratory are supported by the U.S. Department of Energy under contract no. DE-AC02-05CH11231. **Funding:** J.P. and T.H. acknowledge Institutes for Basic Science (IBS-R006-D1). J.P. acknowledges the National Research Foundation of Korea (NRF) grant funded by the Korea government (MSIT) (No. NRF-2017R1C1B2010434, No. NRF-2017R1A5 A1015365, and No. NRF-2019M3E6A1064877), the MOTIE (Ministry of Trade, Industry & Energy), and KRSC (Korea Semiconductor Research Consortium) support program for the development of future semiconductor devices (No. 10080657). B.H.K., J.H., S.K., and J.P. acknowledge support by Samsung Science and Technology Foundation under project number SSTF-BA1802-08 for the development of the reconstruction algorithm. H.E. acknowledges the Australian Research Council (ARC) grant DP170101850 and the National Health and Medical Research Council, Australia, grant APP1125909. C.F.R. acknowledges Early Career Fellowship (APP1122769). P.E. acknowledges U.S. Department of Energy Basic Energy Research Materials Sciences and Engineering Division under Contract No. KC22ZH. A.P.A. acknowledge support by the U.S. Department of Energy, Office of Science, Office of Basic Energy Sciences, Materials Sciences and Engineering Division, under Contract No. DE-AC02-05-CH11231 within the Physical Chemistry of Inorganic Nanostructures Program (KC3103). H.C. and B.H. was supported by the Creative Materials Discovery Program through the National Research Foundation of Korea (NRF) funded by the Ministry of Science and ICT (NRF-2017M3D1A1039287) and the Global Frontier Program through the Global Frontier Hybrid Interface Materials (GFHIM) of National Research Foundation of Korea (NRF) funded by the Ministry of Science and ICT (Project No. 2013M3A6B1078882). **Author contributions:** B.H.K. and J.H. contributed equally to the work. B.H.K., J.H., P.E., H.E., and J.P. planned the research. B.H.K., P.E., and J.P. discussed and/or acquired the data. B.H.K., J.H., S.K., C.R., and H.E. conducted the image reconstruction. B.H.K., J.H., S.K., A.P.A., T.H., P.E., H.E., and J.P. analyzed and interpreted the results. H.C., D.K., H.B., H.L., and B.H. performed the DFT calculations and MD simulations. B.H.K., H.H., and J.L. obtained XRD pattern. B.H.K., J.H., P.E., H.E., and J.P. wrote the manuscript. P.E., H.E., and J.P. supervised the research. All authors contributed to the discussion of results. **Competing interests:** The authors declare no competing financial interests. **Data and materials availability:** All data are available in the main text or the supplementary materials.

**Supplementary Materials:**

Materials and Methods

Figures S1-S24

Tables S1, S2

Movie S1, S2

References (*40-42*)

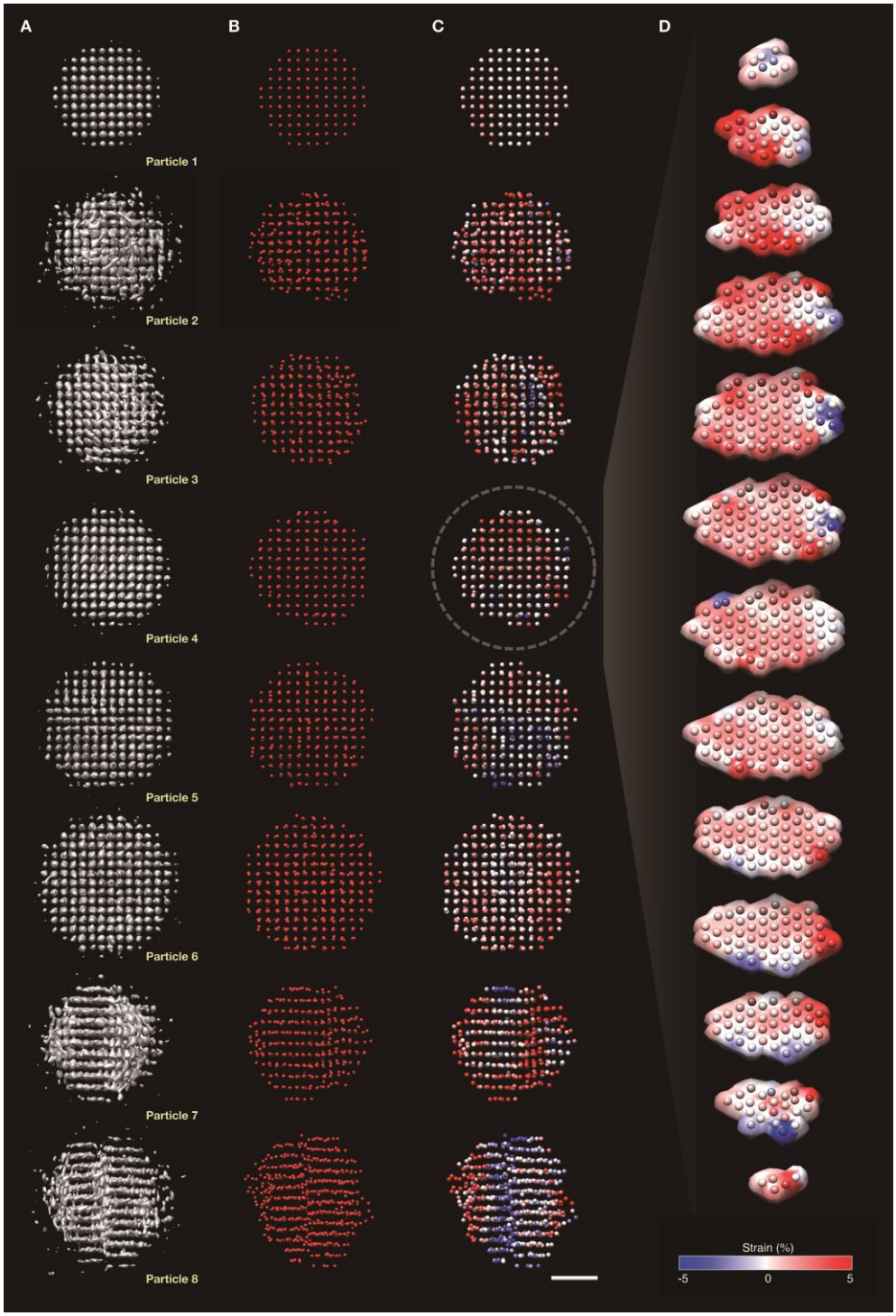


**Fig. 1. Atomic-resolution 3D SINGLE for Pt nanocrystals in solution phase.** (**A**) Isosurfaces of high-resolution 3D density maps, (**B**) atomic position maps, and (**C**) strain ($\varepsilon_{xx}$) maps of 8 individual nanocrystals. (**D**) Sliced images of the strain ($\varepsilon_{xx}$) map of Particle 4. Strain is indicated by color gradient from red (5%), white (0%) to blue (-5%) colors. Scale bar, 1 nm.

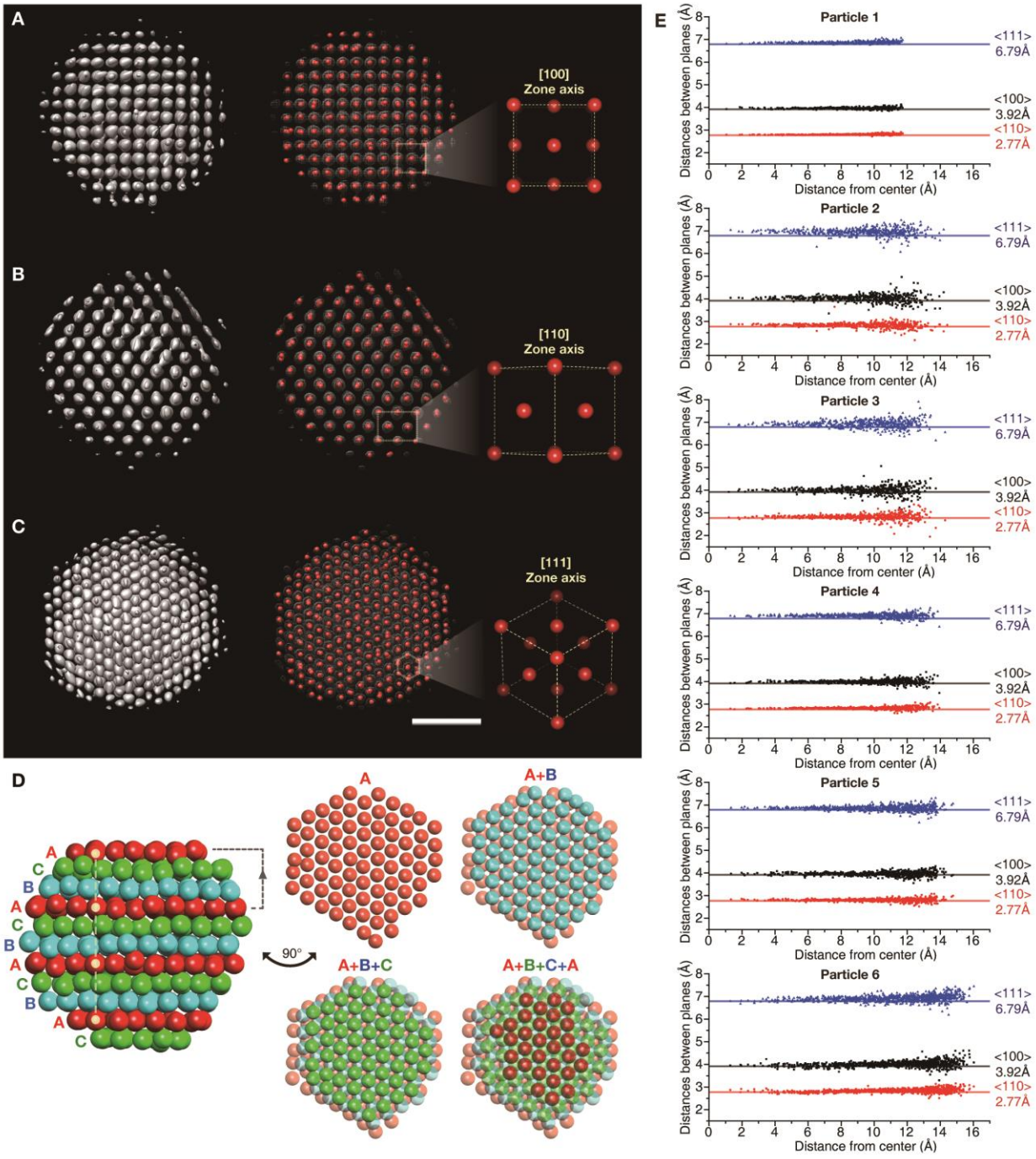


**Fig. 2. Atomic structure analysis of single crystalline Pt nanocrystals reveals progressive disorder close to the surface.** (**A** to **C**) 3D density maps and atomic positions of Particle 4. (**D**) Packing structure of the nanocrystal. (**E**) Interatomic distances in the direction of <110> (red), <100> (black), and <111> (blue) for nanocrystals with six different sizes. Scale bar, 1 nm.

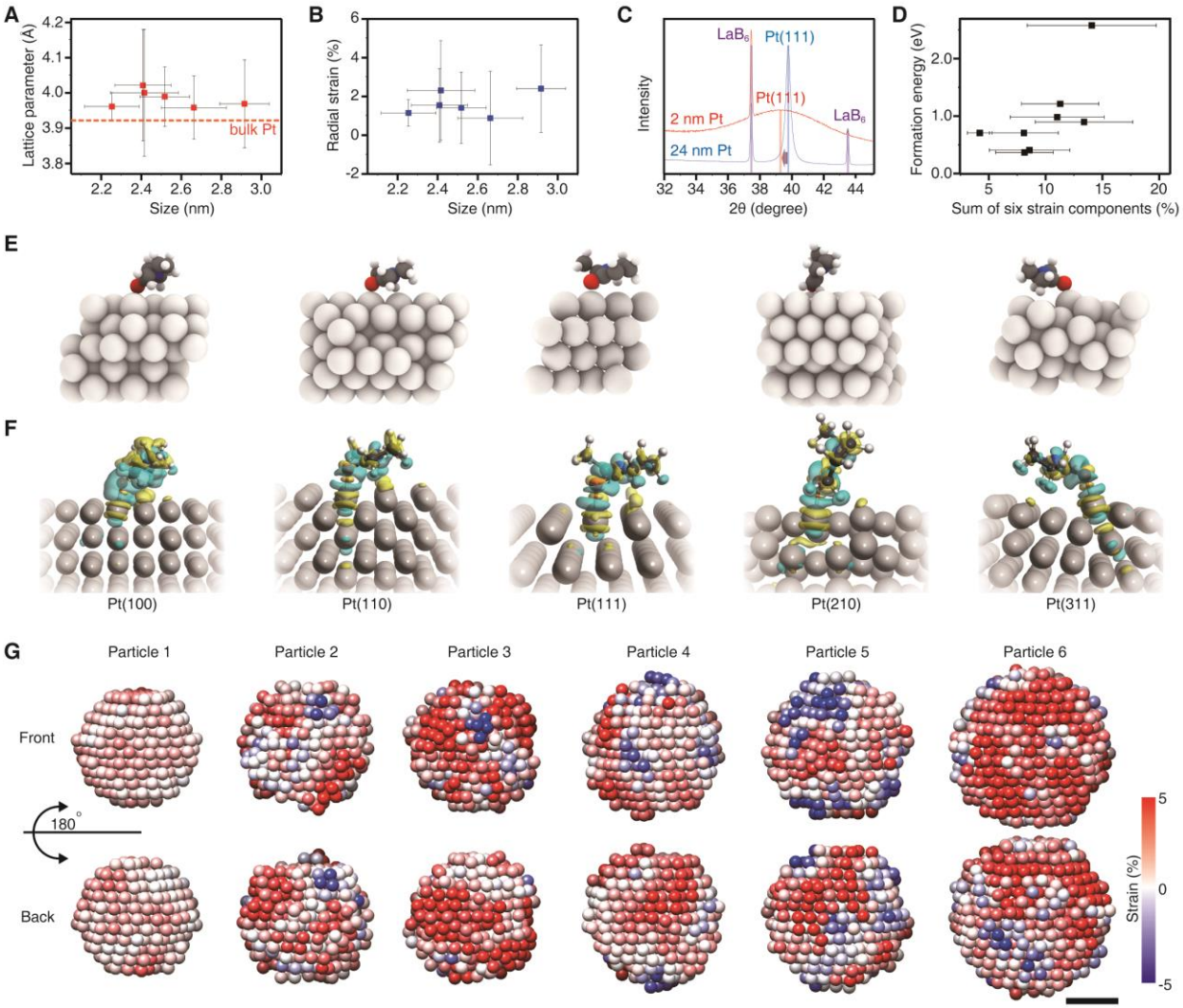


**Fig. 3. Size dependent properties of Pt nanocrystals inferred from their 3D atomic maps.** (**A**) Fitted lattice parameters and (**B**) averaged radial strain values of single crystalline nanocrystals with six different sizes. (**C**) XRD patterns of 2 nm-sized PVP-protected Pt nanocrystals and 24 nm-sized Pt nanocrystals as a reference. (**D**) Formation energy of the reconstructed Pt nanocrystals calculated using their atomic coordinates in a vacuum environment. (**E**) Binding mode of a PVP ligand onto Pt surfaces with five different planes and (**F**) its charge density distributions. Blue color indicates the electron deficient region. (**G**) Radial strain maps of the six single crystalline particles. Strain is indicated by color gradient from red (5%), white (0%) to blue (-5%) colors. Scale bar, 1 nm.

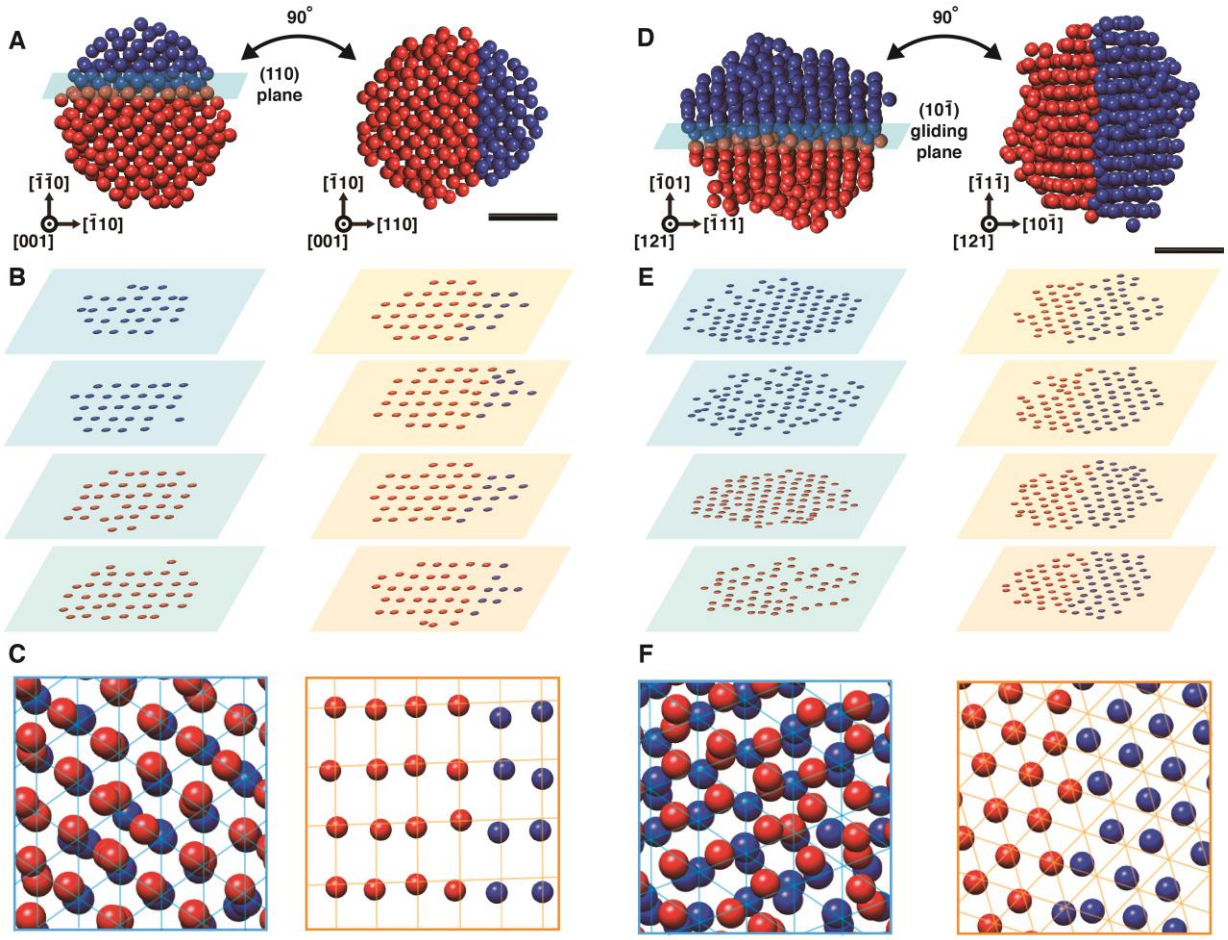


**Fig. 4. 3D structure analysis of nanocrystals that have complicated structures.** (**A** to **C**) 3D structure analysis of a distorted nanocrystal (Particle 7). (A) Overall atomic position map shown along [001]. Red and blue spheres represent atoms of each domain. (B) Sliced planes of (110) (left) and ($\bar{1}$10) (right). (C) Superimposed atomic positions of two layers of each domain (**D** to **F**) 3D structure analysis of a nanocrystal with a dislocation (Particle 8). (D) Overall atomic position map shown along [121]. (E) Sliced planes of (10$\bar{1}$) (left) and ($\bar{1}$1$\bar{1}$) (right) planes. (F) Superimposed atomic positions of two layers of each domain. Scale bars, 1 nm.

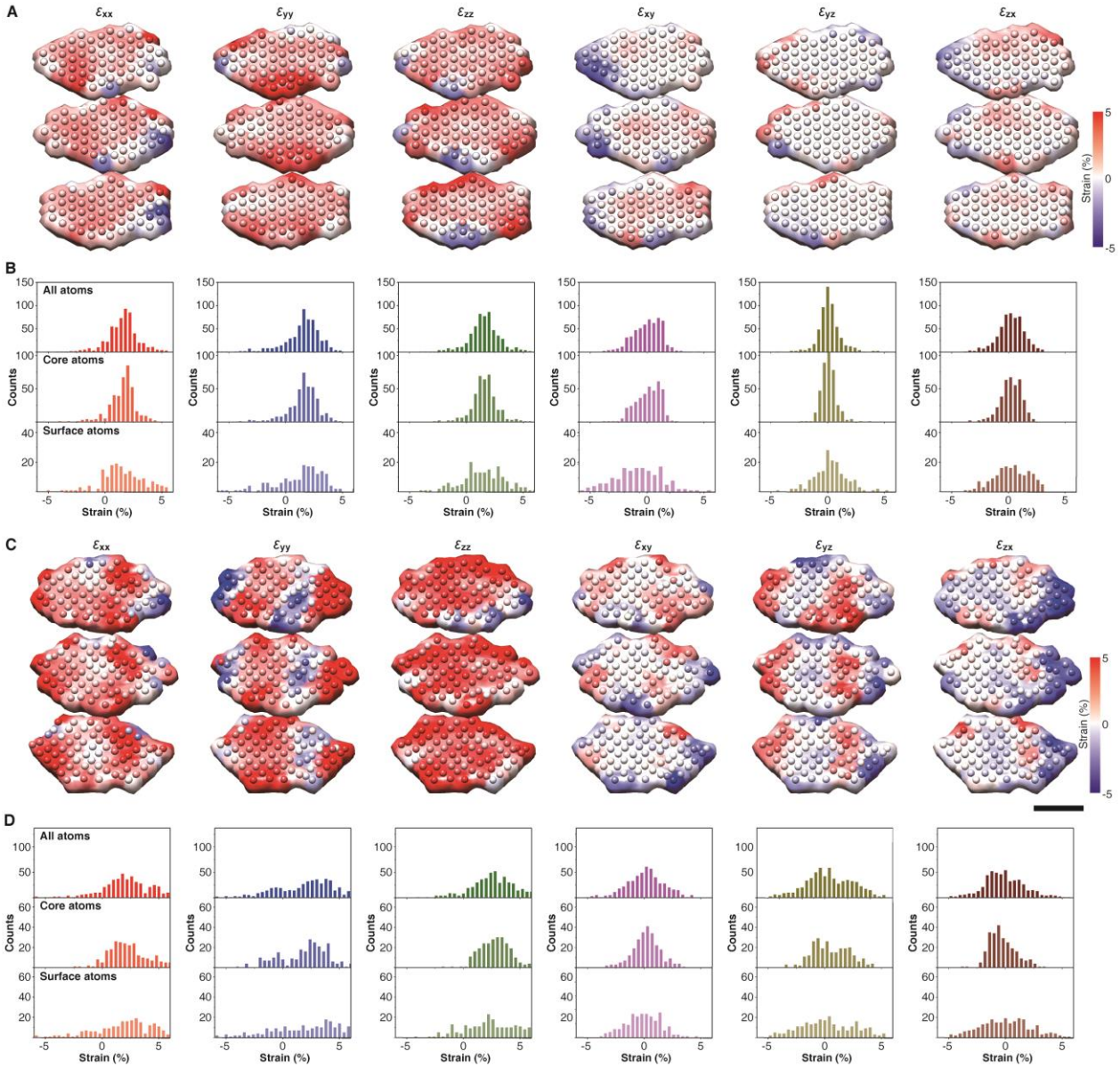


**Fig. 5. 3D strain tensor analysis of Pt nanocrystals.** (**A**) Sliced maps of the six components of the strain tensors for single crystalline particle (Particle 4). (**B**) Histograms of the strain tensors of (top) all atoms, (middle) core atoms, and (bottom) surface atoms of Particle 4. (**C**) Sliced maps of the six components of the strain tensors for particle with distorted lattice (Particle 7). (**D**) Histograms of the strain tensors of (top) all atoms, (middle) core atoms, and (bottom) surface atoms of Particle 7. Strain is indicated by color gradient from red (5%), white (0%) to blue (-5%) colors. Scale bar, 1 nm.

Science
AAAS

# Supplementary Materials for

## Critical differences in 3D atomic structure of individual ligand-protected nanocrystals in solution

Byung Hyo Kim, Junyoung Heo, Sungin Kim, Cyril F. Reboul, Hoje Chun, Dohun Kang, Hyeonhu Bae, Hyejeong Hyun, Jongwoo Lim, Hoonkyung Lee, Byungchan Han, Taeghwan Hyeon, A. Paul Alivisatos, Peter Ercius*, Hans Elmlund*, Jungwon Park*

Correspondence to: percius@lbl.gov, hans.elmlund@monosh.edu, or jungwonpark@snu.ac.kr.

**This PDF file includes:**



**Other Supplementary Materials for this manuscript include the following:**

## Materials and Methods

Synthesis of Pt nanocrystals

Pt nanocrystals of 2 to 3 nm in size were synthesized based on previously reported methods (*40*). 0.05 mmol of $(NH_4)_2Pt(II)Cl_4$ (99.995%, Aldrich), 0.75 mmol of tetramethylammonium bromide (98%, Aldrich), 1 mmol of polyvinylpyrrolidone (PVP, M.W. 29,000, Aldrich), and 10 mL of ethylene glycol were mixed in a three-neck round bottom flask. Then, the mixture was heated to 160 °C and kept for 20 min. After cooling the solution to room temperature, 90 mL of acetone was added to precipitate the particles from the dispersion. The products were then centrifuged at 4,000 rpm for 5 min. The supernatant was discarded and the Pt nanocrystals were collected. The nanocrystals were then redispersed in 5 mM 4-(2-hydroxyethyl)-1-piperazineethanesulfonic acid (HEPES) based buffer solution with pH 7.4.

Preparation of graphene liquid cells

Graphene for liquid cell was synthesized on 25 μm thick copper foil (99.8 %, Alfa Aesar) by chemical vapor deposition (CVD) method. The copper foil in a quartz tube was heated to 1,000 °C for 30 min in hydrogen environment. Graphene was grown onto the copper foil with flows of 25 $cm^3$/min of methane and 10 $cm^3$/min of hydrogen at 1,000 °C. After 20 min, the product was rapidly cooled to room temperature with methane flow.

Graphene TEM (transmission electron microscopy) grids were prepared by transferring the graphene to holey carbon TEM grid using direct transfer method. The graphene covered copper foil was treated in weak oxygen plasma to etch graphene on one side of the foil. A Quantifoil TEM grid (Ted Pella) was placed onto the other side of copper foil, on which graphene was not etched. Then, the copper foil substrate was etched with 0.1 g/mL of ammonium persulfate aqueous solution. The graphene TEM grid was washed with deionized water several times.

A graphene liquid cell was fabricated with two graphene TEM grids. 0.5 μL of Pt nanocrystal solution was loaded onto a graphene TEM grid. The other graphene TEM grid was gently laid on the graphene TEM grid with the liquid sample, so that the liquid samples can be sandwiched by graphene sheets. The sealing of liquid sample can be achieved by strong interaction between two graphene surfaces.

Acquisition of TEM images

TEM movies of Pt nanocrystals in the graphene liquid cell were obtained with 400 frames/s using TEAM I, an FEI Titan 80/300 TEM equipped with a post-specimen geometric- and chromatic-aberration corrector and Gatan K2 IS direct electron detector. Thousands of images with 1,920 × 1,728 pixels and 0.358 Å pixel resolution were acquired at a dose rate of ~15 $e^-/Å^2$·frame at an acceleration voltage of 300 kV. The pixel size was confirmed based on the known lattice spacing of the graphene sheets containing the nanocrystals. TEM images of rotating nanocrystals were used in the 3D reconstruction process. Successful 3D reconstruction of nanoparticles that differ in size, composition, and solvating molecules requires extensive optimization of imaging conditions, image processing, and reconstruction parameters. TEM imaging conditions must be optimized to obtain good signal-to-noise ratio of the 2D projected lattice for a given rotational rate, local thickness of the liquid, and image capture rate.

3D reconstruction

Weighted averaging over five consecutive frames was used to improve the signal-to-noise ratio. Each frame was given a scalar weight based on the correlation to the average. The weighted averaging was repeated by moving one frame step throughout the entire image series, maintaining the original 400 frame/s (figs. S1A and B and movie S1). The number of images used for averaging can be finely controlled for different nanoparticles to ensure that independent lattice information is seen in each averaged TEM image since the local environment of the nanoparticle, such as the thickness of liquid, ligand passivation, and resulting rotational rate, can vary. We estimated the contrast transfer function (CTF) parameters using the CTFFIND4 program. TEM image settings were obtained by tracking nanocrystals based on tracing their center of mass, followed by cropping the particle images to appropriate box sizes. Images were acquired in "black-atom" contrast with slight negative focus and negative spherical aberration coefficient. Thus, contrast inversion of the phase contrast TEM images of nanocrystals was conducted to equate intensity in each pixel to atomic density during the reconstruction process as necessitated by the reconstruction method (fig. S1C). Next, we carried out background subtraction by using neighbor image patches that contain background signal originated from the graphene windows and liquid of the graphene liquid cell. Eight adjacent boxes with a size of ~4 nm around the box containing the nanocrystal were cropped from the entire image stack and integrated independently to generate eight neighboring image stacks. Each stack was then averaged to create eight background images containing signal from the graphene lattice and the liquid. Next, eight image stacks of the nanocrystal were created by subtracting the eight background images from the raw box image stack containing the nanocrystal. We selected the background subtracted stack including minimal graphene peaks for further processing. 3D density maps of Pt nanocrystals were reconstructed using the PRIME algorithm (*24*). Pt face centered cubic (fcc) structure with cuboctahedron shape was used as an initial model. The first 3D structure was obtained with relatively low angular sampling (1,000 projection directions) and then refined using 3,000 directions. After refinement, Coulomb charge 3D density maps were obtained and used for further analysis, such as atomic position assignment and strain mapping. The reconstruction process is robust for datasets that include enough lattice information and orientation coverage.

**Supplementary Text**

Atomic position assignment

The 3D positions of the individual atoms were assigned by identifying local maxima in density maps and discarding ones originated from background noise for each 3D atomic-resolution map (figs. S3 and S4). At first, local maxima in density maps were identified. Then, the selected local maxima were sorted according to intensity value and atomic positions were selected from the upper boundary in the intensity distribution profile. The cutoff was determined by the nanocrystal radius. The Bohr radius of Pt (1.77 Å) was applied as a minimum peak distance to adjacent local maxima to remove shoulder peaks. A local maximum that shows lower intensity in a pair with a distance below the Bohr radius was discarded. Local maxima that are presumably originated from the arbitrary background signal from the liquid around the particle were removed by applying threshold limit in terms of coordination number. We selected atomic positions with the coordination number greater than four.

Measuring interatomic distances for each direction

Interatomic distance for specific direction was assigned as distance between one atom and its neighbor atom located with the shortest distance from the ideal point along the direction. The assigned interatomic distances in the direction families (<110>, <100>, and <111>) are geometrically averaged from those along constituent directions (e.g. [100], [$\bar{1}$00], [010], [0$\bar{1}$0], [001], and [00$\bar{1}$] for <100>).

Strain mapping using lattice fitting

Strain was calculated through differentiation of displacement field (*38*). In this method, displacement field at each atom was acquired by subtracting ideal atomic position from real atomic position and interpolated using kernel density estimation (*17*).

For crystal structure analysis, three normal vectors, $n_x$, $n_y$, and $n_z$, and relative positions of atoms, $a_i$, $b_i$, and $c_i$ ($a_i, b_i, c_i \in Z$), were determined with lattice fitting. Ideal atomic position, $r_{\mathrm{ideal},i}$, from real atomic position, $r_{\mathrm{real},i}$, were described as follows,

$$r_{\mathrm{real},i} = a_i n_x + b_i n_y + c_i n_z + e_i \quad (1)$$

$$r_{\mathrm{ideal},i} = a_i n_{0x} + b_i n_{0y} + c_i n_{0z} \quad (2)$$

where $e_i$ is residual of the fitting, and $n_{0x}$, $n_{0y}$, and $n_{0z}$ are normal vectors with size as a half Pt unit cell, 1.96 Å. Twice of $n_x$, $n_y$, and $n_z$ were assigned to be three components of the lattice parameter. Representative lattice parameters, shown in Fig. 3A, were defined as geometric mean of the three components.

Displacement field of each atom, $u_i$, can be calculated by using following equation.

$$u_i = r_{\mathrm{real},i} - r_{\mathrm{ideal},i} \quad (3)$$

After calculating displacement of each atom, 3D Gaussian distribution was weighted to generate continuous function, $u(r)$.

$$u(r) = \frac{\sum_i u_i \exp(-\frac{{D_i}^2}{2\sigma^2})}{\sum_i \exp(-\frac{{D_i}^2}{2\sigma^2})} \quad (4)$$

Where $r$ is position vector, $D_i = \left| r - r_{\mathrm{real},i} \right|$, and $\sigma$ is the standard deviation of 3D Gaussian kernel. A standard deviation of 2 Å was chosen based on leave-one-out cross-validation (LOOCV) (fig. S21) (*41*). Six 3D strain components were finally calculated from three components of displacement field vector, which are $u_x$, $u_y$ and $u_z$, by using Equation 5 and 6.

$$\epsilon_{xx} = \frac{\partial u_x}{\partial x}, \epsilon_{yy} = \frac{\partial u_y}{\partial y}, \epsilon_{zz} = \frac{\partial u_z}{\partial z} \quad (5)$$

$$\epsilon_{xy} = \frac{1}{2}(\frac{\partial u_x}{\partial y} + \frac{\partial u_y}{\partial x}), \epsilon_{yz} = \frac{1}{2}(\frac{\partial u_y}{\partial z} + \frac{\partial u_z}{\partial y}), \epsilon_{zx} = \frac{1}{2}(\frac{\partial u_z}{\partial x} + \frac{\partial u_x}{\partial z}) \quad (6)$$

$\epsilon_{xx}$, $\epsilon_{yy}$, and $\epsilon_{zz}$ represents elongation of lattice, along with $x$, $y$, and $z$ direction, respectively. $\epsilon_{xy}$, $\epsilon_{yz}$, and $\epsilon_{zx}$ represents lattice deformation involving change of angles, $\gamma$, $\alpha$, and $\beta$, respectively.

Radial strain was also calculated by using similar approach. Radial displacement field, $u_r$, and radial strain component, $\epsilon_{rr}$, were described as follows,

$$u_{i,r} = |r_{\text{real},i} - r_c| - |r_{\text{ideal},i} - r_c| \quad (7)$$

$$\epsilon_{rr} = \frac{\partial u_r}{\partial r} \quad (8)$$

where $r_c$ is the position of the center of mass, and $u_{i,r}$ is radial displacement field of $i$ th atom.

Strain mapping using geometric phase analysis (GPA)

Strain at each atom was measured using 3D extended GPA (*38*). First, intensity profile, $I(r)$, was generated from atomic position map with 'pdb2mrc' program in EMAN. Phase images, $P_g(r)$, were then calculated from intensity profile and reciprocal vector from Pt fcc lattice, $g$, using following a series of equations,

$$\tilde{H}_g(k) = \tilde{I}(k+g)\tilde{M}(k) \quad (9)$$

$$H'_g(r) = H_g(r)\exp\{2\pi i g \cdot r\} \quad (10)$$

$$P_g(r) = \text{Phase}[H'_g(r)] - 2\pi g \cdot r \quad (11)$$

where $\tilde{I}(k)$ is the Fourier transform of $I(r)$, $H_g(r)$ is Fourier coefficient as function of $r$, and $\tilde{H}_g(k)$ is Fourier transform of Fourier coefficient. Three phase images, $P_{g1}(r)$, $P_{g2}(r)$, and $P_{g3}(r)$, were obtained from three nonlinear different reciprocal vectors, $g_1$, $g_2$, and $g_3$. Relationship between three-dimensional displacement fields and phase images was described by the equations below.

$$P_{g1}(r) = -2\pi g_1 \cdot u(r) = -2\pi\{g_{1x}u_x(r) + g_{1y}u_y(r) + g_{1z}u_z(r)\} \quad (12)$$

$$P_{g2}(r) = -2\pi g_2 \cdot u(r) = -2\pi\{g_{2x}u_x(r) + g_{2y}u_y(r) + g_{2z}u_z(r)\} \quad (13)$$

$$P_{g3}(r) = -2\pi g_3 \cdot u(r) = -2\pi\{g_{3x}u_x(r) + g_{3y}u_y(r) + g_{3z}u_z(r)\} \quad (14)$$

where $g_{ix}$, $g_{iy}$, and $g_{iz}$ are $k_x$, $k_y$, and $k_z$ components of the reciprocal vector $g_i$, respectively, and $u_x(r)$, $u_y(r)$, and $u_z(r)$ are the $x$, $y$, and $z$ components of the 3D displacement field, $u(r)$, respectively. 3D displacement field can be calculated by combining Equation 12, 13, and 14 to matrix form and taking the inverse of the matrix with reciprocal vectors.

$$\begin{bmatrix} u_x \\ u_y \\ u_z \end{bmatrix} = -\frac{1}{2\pi}\begin{bmatrix} g_{1x}g_{1y}g_{1z} \\ g_{2x}g_{2y}g_{2z} \\ g_{3x}g_{3y}g_{3z} \end{bmatrix}^{-1}\begin{bmatrix} P_{g1} \\ P_{g2} \\ P_{g3} \end{bmatrix} \quad (15)$$

Six 3D strain components as a function of position were finally calculated by using Equation 5 and 6.

Multi-slice TEM simulation

Simulated TEM images used in validation processes (figs. S7 to S11) were obtained by using multi-slice simulation (*26*). Simulated TEM images of an ideal Pt lattice with sizes of 2.5 nm and 4.0 nm (figs. S7 and S8) were extracted by randomly rotating ideal Pt atomic coordinates 5,000 times and placing rotated coordinates within a 57.28 Å (160 pixels × 0.358 Å/pixel) cubic super cell. The super cells were splitted into multiple 1.5-Å-thick slices along the z-axis, with 160 × 160 pixels sampling in the *x* and *y* axis. The following input parameters were used for the simulations: acceleration voltage of 300 kV, mean, standard deviation and sampling size of defocus distribution of 50, 40 and 10 Å, $C_3$ aberration of -0.01 mm, $C_5$ aberration of 3 mm, objective aperature of 30 mrad, minimum and maximum illumination angle of 0 and 1 mrad, thermal temperature of 273 K thermal, and a number or thermal vibration configurations of 5. Noise was added to give a final signal-to-noise ratio of 0.2. The TEM images generated by the multi-slice simulation were used for 3D reconstruction to validate the 3D SINGLE process (figs. S7 to S11). The simulation and reconstruction process was also conducted using smaller pixel size of 0.0895 Å (640 × 640 pixels) to demonstrate imaging conditions with electron beam and sample (figs. S9, and S11). In this case, the 640 × 640 pixels in the simulated images were binned to 160 × 160 pixels (fig. S9, A to H) or 320 × 320 pixels (fig. S9, I to L) by summing the intensity to demonstrate different pixel resolutions in detector. The reconstructed 3D maps were compared with the original maps by calculating root mean square deviation,

$$\sigma = \frac{1}{\sqrt{2}N_i}\sum_i \sqrt{(a_{xi}-b_{xi})^2+(a_{yi}-b_{yi})^2+(a_{zi}-b_{zi})^2}$$

where $N_i$ is number of atoms of the particle, $a_{xi}$ is *x* coordinates of *i*th atoms in the original particle, and $b_{yi}$ is *y* coordinates of *i*th atoms in the reconstructed particle. It is worth noting that the precision is not proportional to the orderness of nanocrystals.

To compare our 3D reconstruction result with the original TEM images, simulated TEM images were calculated by rotating the eight atomic maps in the direction of projection assigned by 3D reconstruction algorithm (figs. S12 and S13). Rotated atomic maps were placed within coordinates within a 57.28 Å (160 pixels × 0.358 Å/pixel) cubic super cell and 2D images simulated as described above. Simulated TEM images for re-reconstruction (fig. S14) were calculated in the same way.

The validation of 3D SINGLE in more realistic condition was conducted by reconstruction of multi-slice TEM images of model Pt nanocrystal in a graphene liquid cell. In the liquid cell, single layered graphene sheets are located on the top and bottom of water layer with a thickness of 10 nm. The atomic coordinates of water were obtained by molecular dynamic simulation using the Large-scale Atomic/Molecular Massively Parallel Simulator (LAMMPS) package. A CHARMM force field and TIP3P water model were employed for the simulation. 10968 water molecules were randomly created inside the 57.28 Å × 57.28 Å × 100.0 Å simulation box. After implementation of energy minimization to stabilize the system, NVT ensemble with 1 fs time step and Nosé-Hoover thermostat was performed for 100 ps, and water trajetories were recorded every 100 fs. TEM images of the atomic models including nanocrystal, water, and graphene were obtained via multi-slice simulation with the same parameters. Each multi-slice simulated TEM image includes different random orientation of a nanocrystal and set of geometries of water molecules. Simulated TEM imges reflect continuous rotation of the nanocrystal and fluctuations of water molecules during TEM imaging. After adding Gaussian noise with a signal-to-noise ratio of 0.5, the TEM images were used for reconstruction for validation (figs. S10 and S11).

X-ray diffraction (XRD) measurement

Samples for XRD measurements were prepared by mixing PVP-passivated 2 nm-sized Pt nanocrystals with lanthanum hexaboride ($LaB_6$, Aldrich) and 24 nm-sized Pt particles (Aldrich) with $LaB_6$ in the ratio of 20:1 and 5:1, respectively. $LaB_6$ was added as an internal calibrant for quantitative analysis of Bragg angles. X-ray diffraction experiments were performed with a monochromatic radiation ($\lambda$ = 1.54595 Å) at the 3D XRS beamline of Pohang Light Source II (PLS-II), Korea. The scattering patterns were detected by the imaging plate with an irradiation time of 3 s. The position and broadening of the Pt(111) XRD peaks were fitted by Gaussian curve after subtracting the background.

The Pt(111) peak position in the XRD pattern of 2 nm-sized nanocrystals is 39.21° and the full width at half maxima (FWHM) is 5.10° obtained by Gaussian fitting, indicating that the Pt nanocrystals have a lattice parameter of 3.976 Å and a grain size of 1.65 nm. The XRD pattern of the reference Pt particles represents a lattice parameter of 3.921 Å, which is close to that of bulk Pt.

Computational Details

We utilized first principles density functional theory (DFT) calculations as implemented in Vienna ab-initio simulation package (VASP) with the Perdew-Burke Ernzerhof (PBE) generalized gradient approximation (GGA) exchange-correlation functional and the projector-augmented wave (PAW) pseudopotentials. The basis plane waves were expanded with cutoff energy of 520 eV. We included the spin polarization correction and van der Waals (vdW) interaction with DFT-D3 method by Grimme (*42*). Formation energy of observed nanoparticles were calculated with the single point electronic relaxation. All atomic positions were fixed with the 3D-reconstruction data. Only Γ-point scheme was used for the nanoparticle calculations, and the vacuum space was imposed to secure 10 Å within the periodic images for each system. The formation energy ($\Delta E$) was calculated as equation below.

$$\Delta E = \frac{1}{N_i}(E_i - E_{pt}N_i) \qquad (16)$$

where $N_i$ is the number of platinum atoms, $E_i$ is the total energy of nanocrystal, and $E_{Pt}$ is the bulk binding energy. In order to calculate the surface energy, we used symmetric supercell slab models with a vacuum space of 15 Å. The Pt slabs with the Miller-index of (100), (110) and (111) were composed of 7 atomic layers and relaxed with 3 inner-most atomic layers fixed and Γ-centered 13×13×1, 13×7×1 and 7×7×1 *k*-point schemes, respectively. For the high Miller-index of Pt(211) and Pt(310) were composed of 16 atomic layers with 4 inner-most atomic layers fixed, and 21 atomic layers with 5 inner-most atomic layers fixed, respectively. The Brillouin-zone integrations for Pt(211) and Pt(310) slabs were performed using Γ-centered 7×9×1 and 13×5×1 *k*-point schemes, respectively. The surface energy ($\gamma_{claen}$) was calculated as equation 17.

$$\gamma_{claen} = \frac{1}{2A}(E^i - N_i E_{bulk}) \qquad (17)$$

where $A$ is the surface unit area of the slab model, $E^i$ is the total energy of the Pt slab with the Miller-index of $i$, $N_i$ is the corresponding number of Pt atoms in the slab and $E_{bulk}$ is the total energy of Pt bulk. For calculating the adsorption energy ($E_{ads}$) of a PVP molecule on Pt surfaces we identified 20 Å of vacuum space was an optimal value for the slab models on the aspects of computational cost and accuracy of energy outcome. The supercell sizes of Pt(100), Pt(110),

Pt(111), Pt(211) and Pt(310) were 3×3×1 with 5 atomic layers and 2 bottom-most atomic layers fixed, 3×3×1 with 7 atomic layers and 3 bottom-most atomic layers fixed, 4×4×1 with 5 atomic layers and 2 bottom-most atomic layers fixed, 4×2×1 with 12 atomic layers and 3 bottom-most atomic layers fixed, and 3×2×1 with 14 atomic layers and 4 bottom-most atomic layers fixed, respectively. The Γ-centered 3×3×1 *k*-point scheme was used for all slab models. PVP ligand was simulated with a monomer of 1-ethyl-2-pyrrolidone and the Brillouin-zone was integrated using Γ-point only. The absorption energy ($E_{ads}$) was calculated with equations 18.

$$E_{ads} = \frac{1}{A}\left(E_{PVP}^{i} - E_{slab} - N_{PVP}E_{PVP}\right) \quad (18)$$

where $E_{PVP}^{i}$ is the total energy of slab with adsorbed PVP and the Miller-index of $i$, $N_{PVP}$ is the number of adsorbed PVP on the slab, $E_{slab}$ is the total energy of the clean slab, and $E_{PVP}$ is the total energy of the PVP. Different adsorption sites for each facet were probed as shown in fig. S19A and table S2.

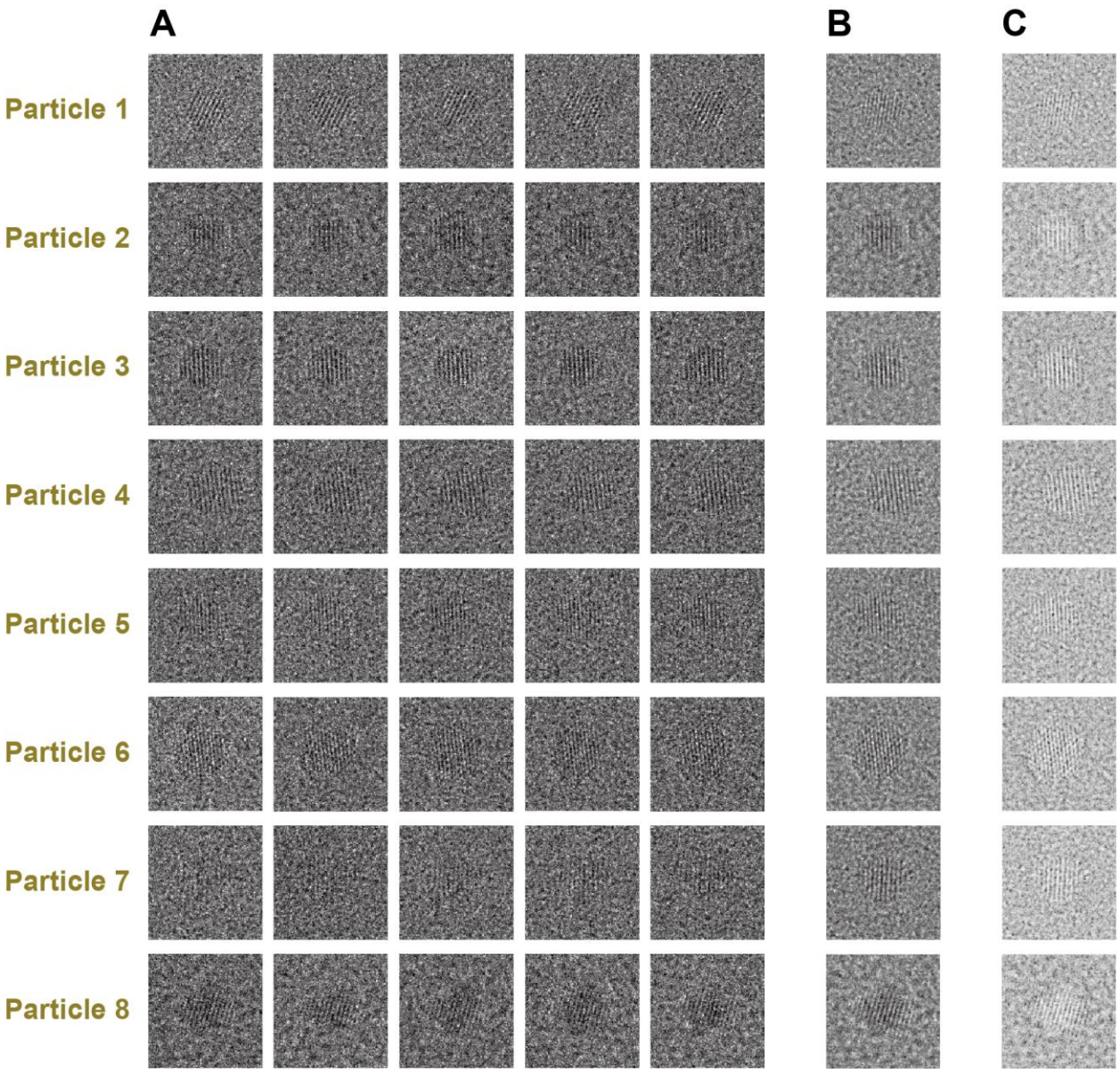


**Fig. S1.**
(**A**) Five consecutive TEM images before averaging of eight nanocrystals shown in Fig. 1. (**B**) Weighted averaged TEM images of the five consecutive images. (**C**) Contrast-inverted TEM images of the averaged images.

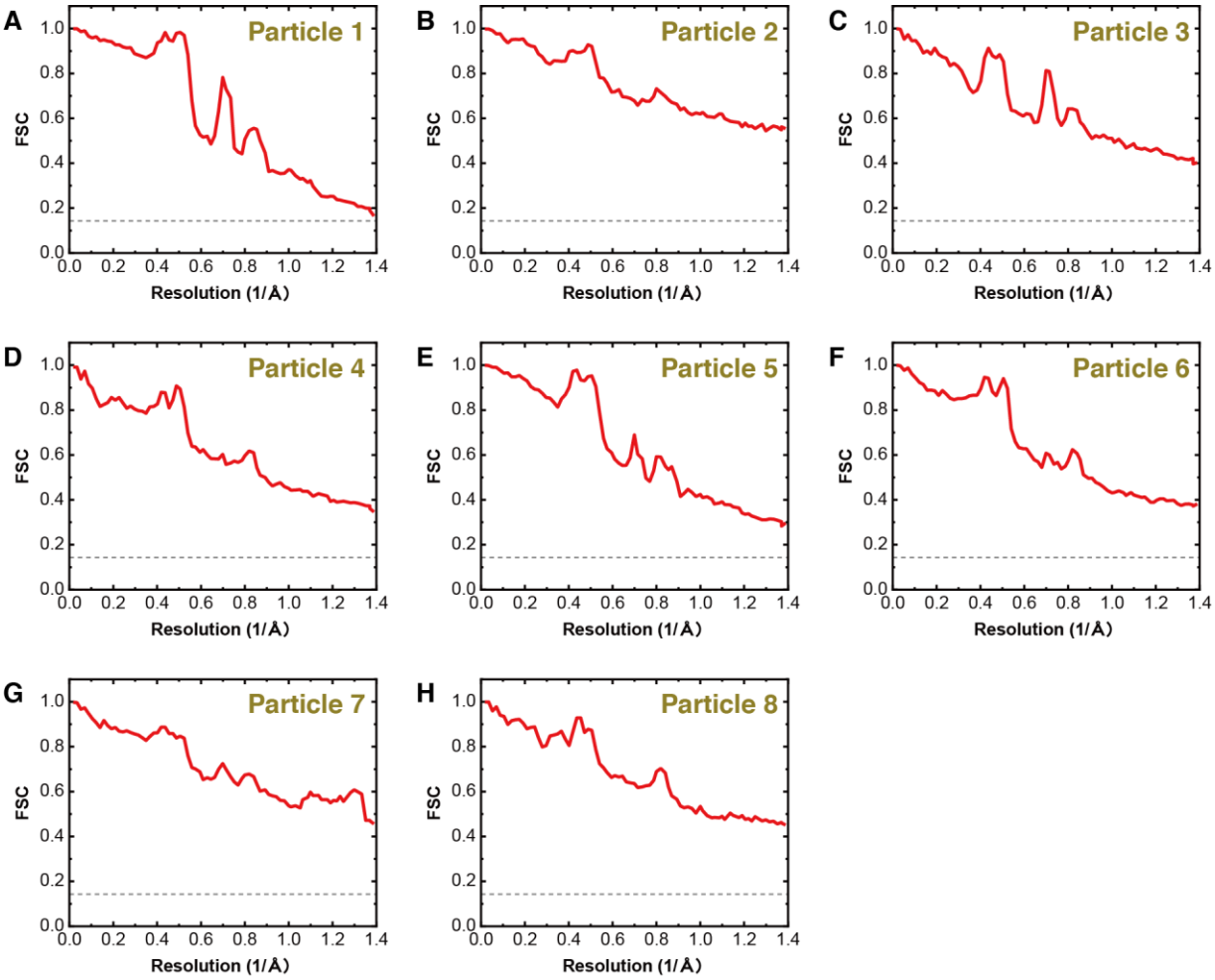


**Fig. S2.**
Fourier shell correlation (FSC) between a 3D density map from odd-frames and a map from even-frames. (**A** to **F**) single crystalline particles, (**G**) particle with distorted crystal, (**H**) particle with dislocation.

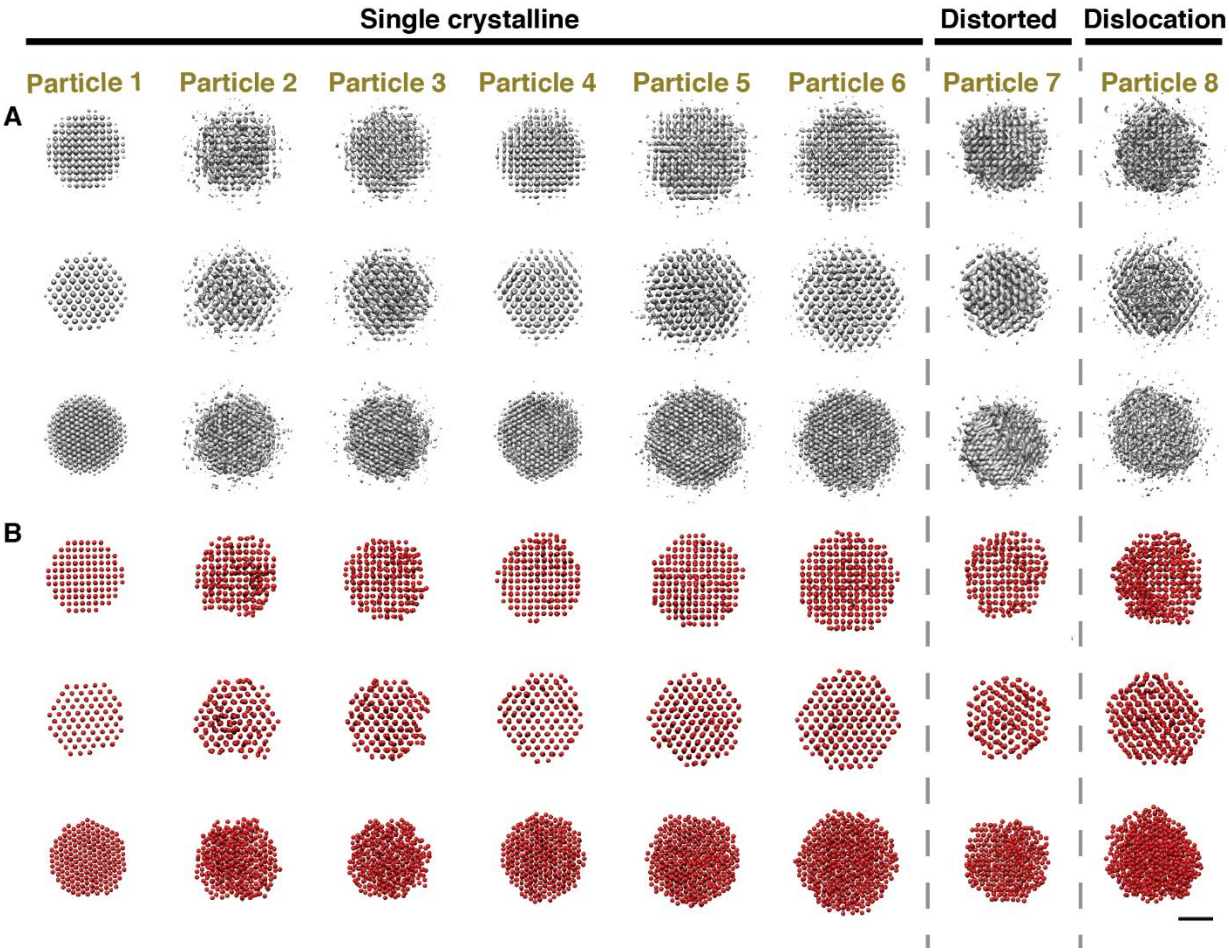


**Fig. S3.**

(**A**) 3D density maps and (**B**) atomic position maps of eight Pt nanocrystals with the zone axis of (top) [100], (middle) [110], and (bottom) [111]. Scale bar, 1 nm.

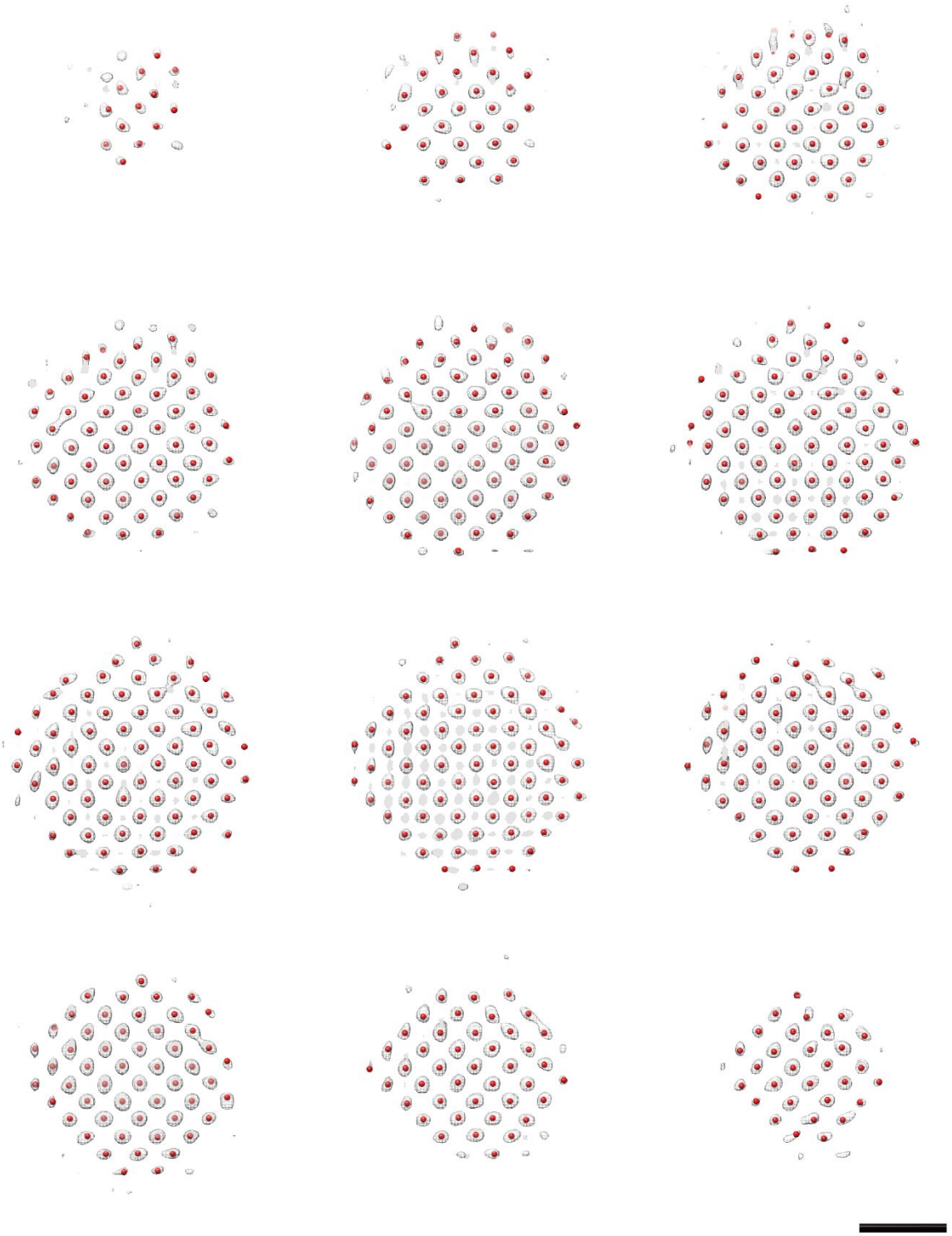

**Fig. S4.**
Sliced images of the density map (white mesh) and the atomic coordinates (red points) of Particle 4. Scale bar, 1 nm.

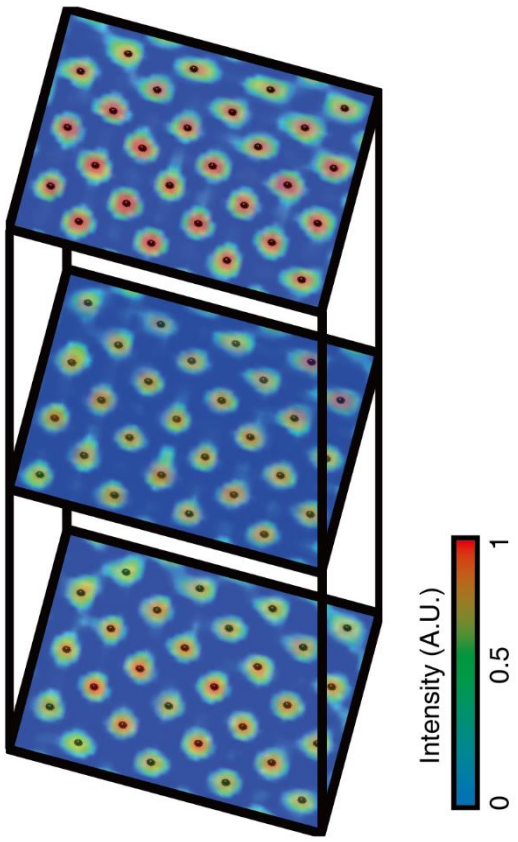


**Fig. S5.**
Representative sliced images of colored density map and allocated atomic positions (black points) of Particle 4.

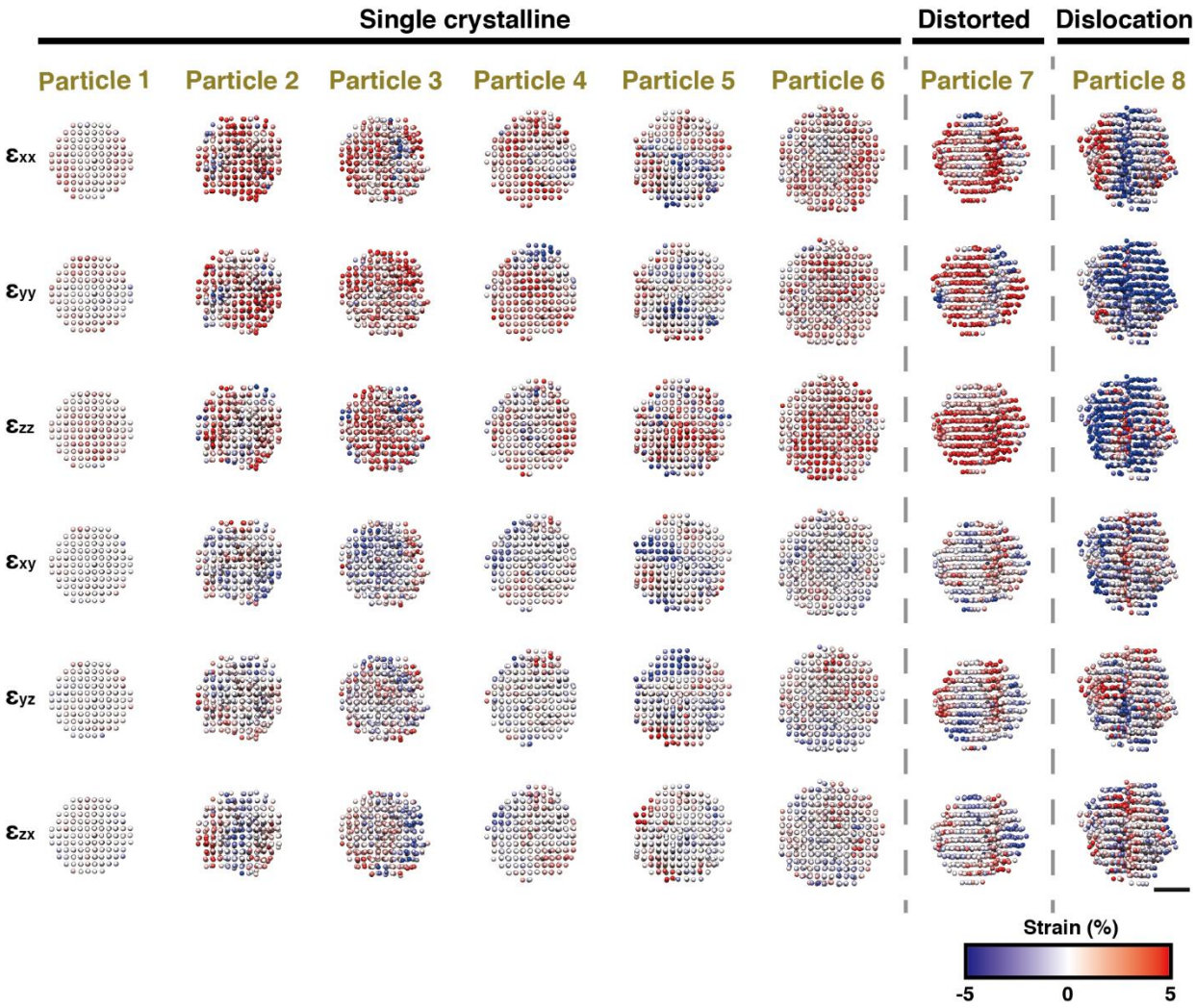


**Fig. S6.**
Six components of 3D strain tensors of eight reconstructed Pt nanocrystals. Strain is indicated by color gradient from red (5%), white (0%) to blue (-5%) colors. Scale bar, 1 nm.

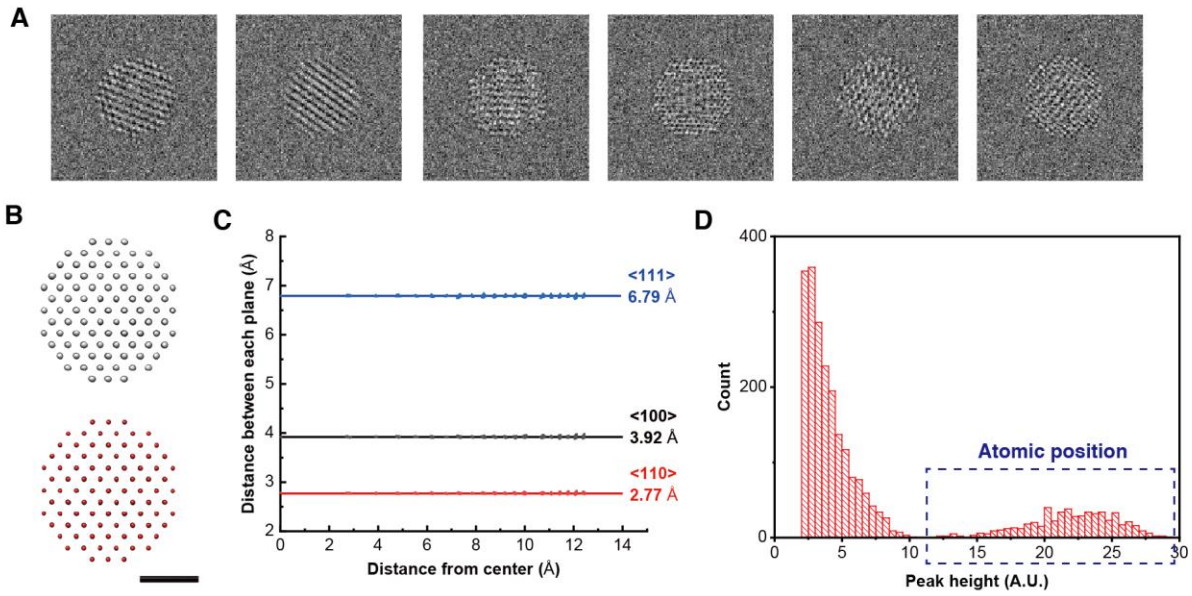


**Fig. S7.**
(**A**) Simulated TEM images from a 2.5 nm-sized Pt nanocrystal having ideal fcc coordinate. (**B**) 3D volume map and atomic position map reconstructed from the simulated TEM images of the ideal Pt nanocrystal. (**C**) Depth profile of interatomic distances in the direction of <110> (red), <100> (black), and <111> (blue) acquired from the 3D atomic position map. (**D**) Peak intensity distribution of the reconstructed volume map. The distribution shows distinct separation between true atom peak and artifacts. Scale bar, 1 nm.

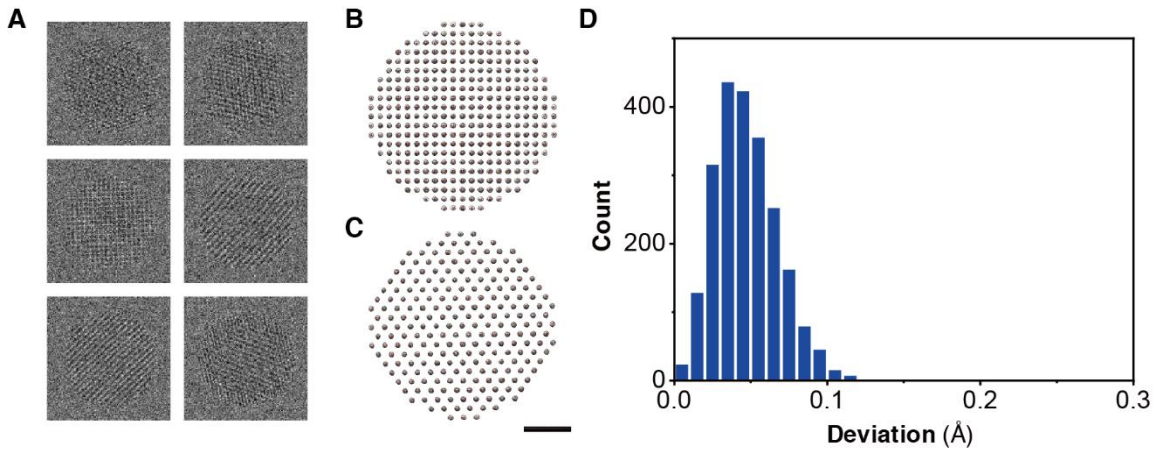


**Fig. S8.**

(**A**) Simulated TEM images from a model 4.0 nm-sized Pt nanocrystal having ideal fcc coordinate. (**B** and **C**) 3D volume maps overlaid with atomic position maps reconstructed from the simulated TEM images with zone axes of (**B**) [100] and (**C**) [110]. (**D**) Distributions of atomic position deviations, showing a root mean square deviations of 4.7 pm. Scale bar, 1 nm.

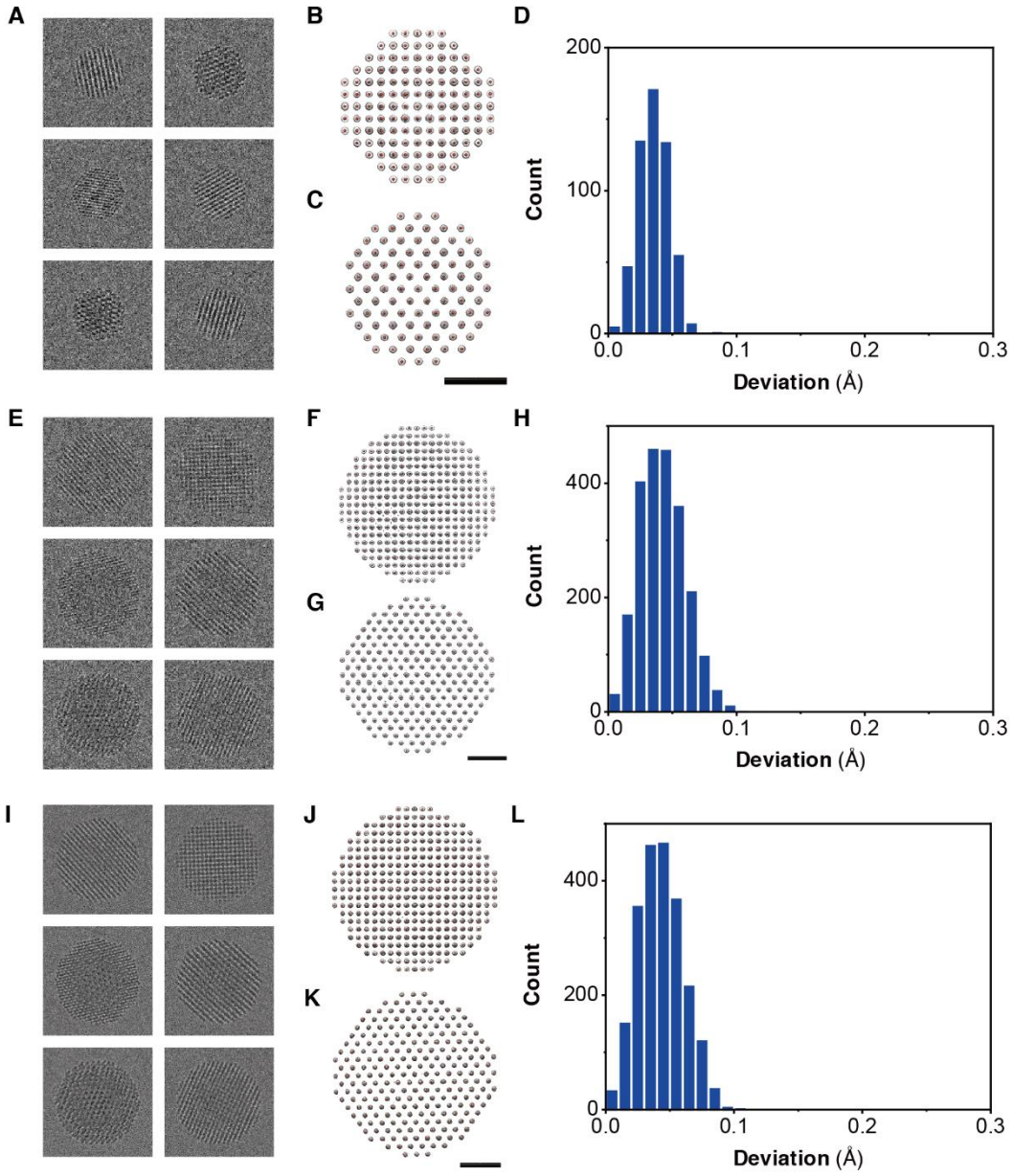


**Fig. S9.**

(**A** to **H**) 3D reconstruction of model Pt nanocrystals with sizes of (**A** to **D**) 2.5 nm and (**E** to **H**) 4.0 nm from multi-slice simulation with a pixel size of 0.0895 Å followed by binning to 0.358 Å by summing intensities. (**I** to **L**) 3D reconstruction of a model 4.0 nm-sized Pt nanocrystal from multi-slice simulation with a pixel size of 0.0895 Å followed by binning to 0.179 Å by summing intensities. (**A**, **E**, and **I**) Multi-slice simulated TEM images of model nanocrystals. (**B**, **C**, **F**, **G**, **J**, and **K**) 3D volume maps overlaid with atomic position maps reconstructed from the simulated TEM images with zone axes of (**B**, **F**, and **J**) [100] and (**C**, **G**, and **K**) [110]. The reconstruction maps are obtained with a parameter of 1,000 projection directions. (**D**, **H**, and **L**) Distributions of atomic position deviations, showing a root mean square deviations of (**D**) 3.5 pm, (**H**) 4.2 pm, and (**L**) 4.3 pm. Scale bars, 1 nm.

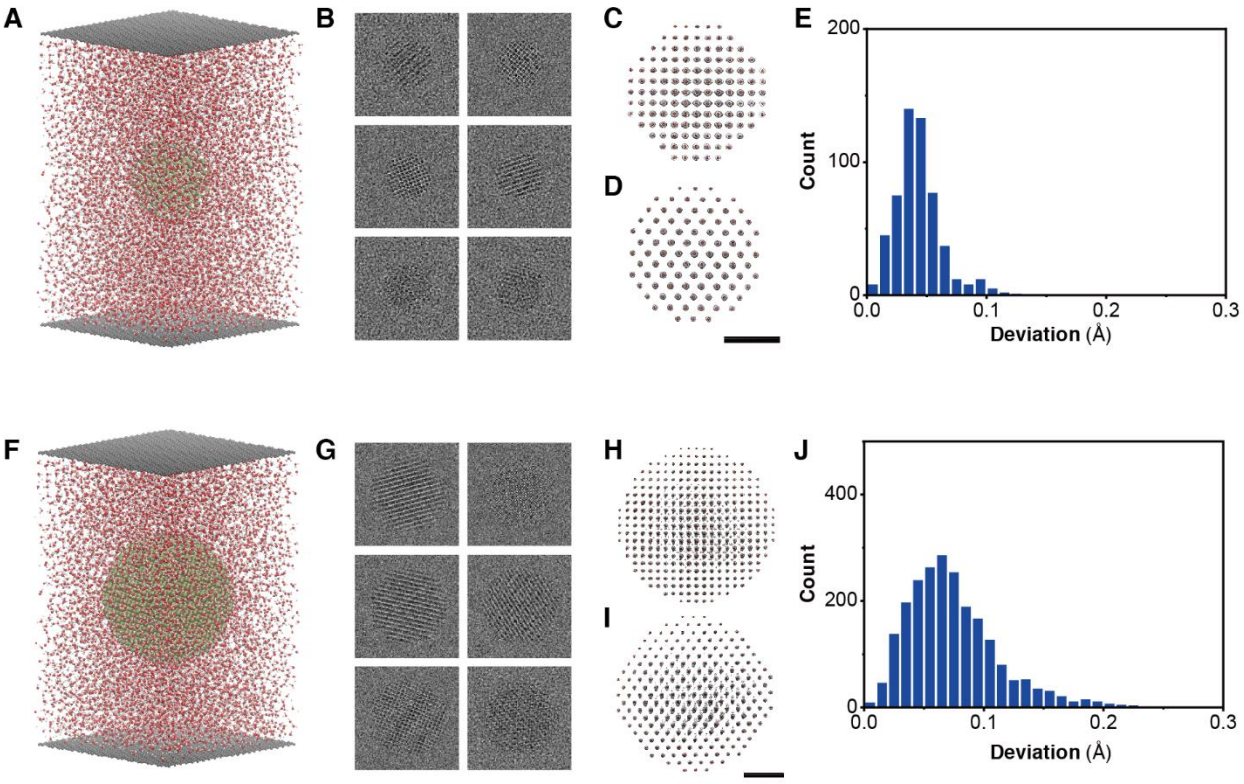


**Fig. S10.**

(**A** and **F**) Atomic models of Pt nanocrystals in graphene liquid cells with a thickness of 10 nm. Red: oxygen, gray: hydrogen, black: carbon, and yellow: platinum. (**B** and **G**) TEM images of the atomic models composed of nanocrystals, liquid, and graphene generated by multi-slice simulation. (**C**, **D**, **H**, and **I**) 3D volume maps and atomic position maps reconstructed from the simulated TEM images with zone axes of (**C** and **H**) [100] and (**D** and **I**) [110]. (**E** and **J**) Distribution of atomic position deviation, showing a root mean square difference of 4.3 pm for 2.5 nm and 7.5 pm for 4.0 nm particle. (**A** to **E**) 2.5 nm-sized Pt nanocrystal and (**F** to **J**) 4.0 nm-sized Pt nanocrystal. Scale bars, 1 nm.

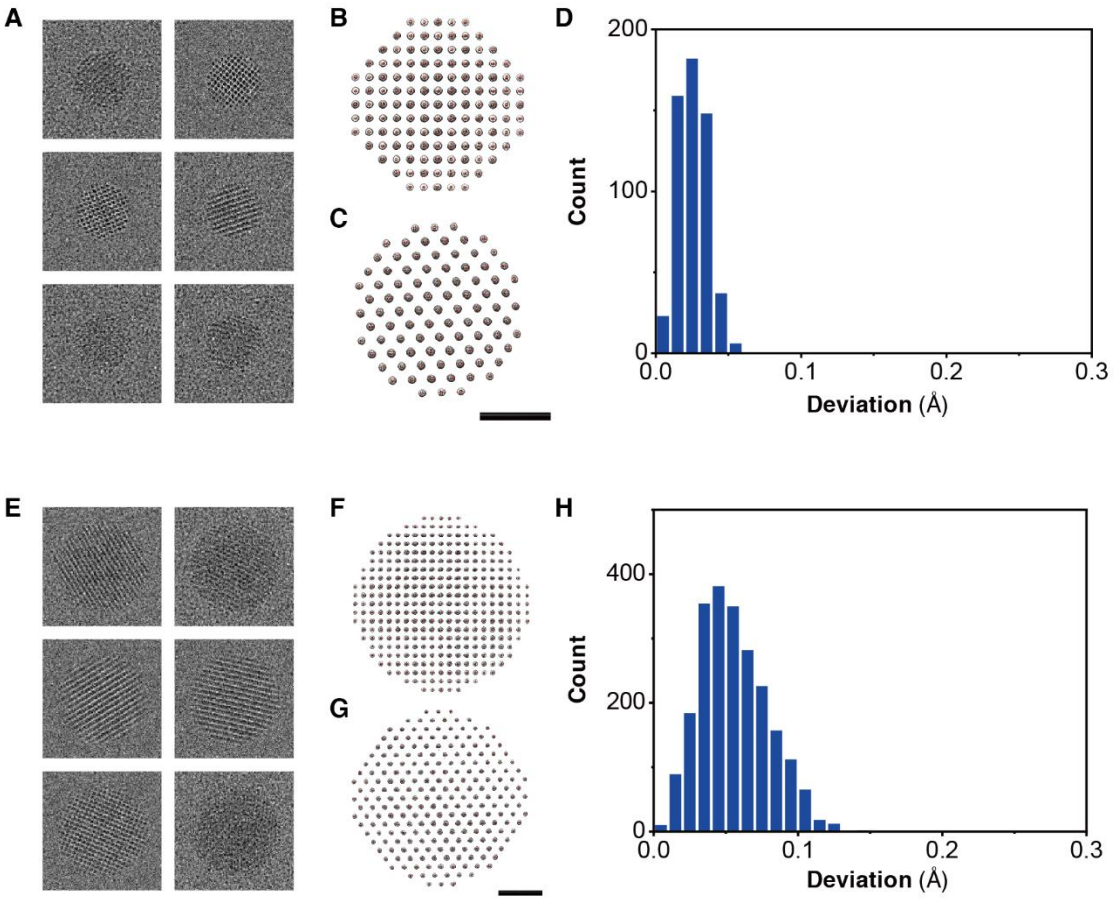


**Fig. S11.**

(**A** and **E**) TEM images of model (**A**) 2.5 nm- and (**E**) 4.0 nm-sized nanocrystals in 10 nm-thick graphene liquid cells from multi-slice simulation with a pixel size of 0.0895 Å followed by binning to 0.358 Å by summing intensities. (**B**, **C**, **F**, and **G**) 3D volume maps overlaid with atomic position maps reconstructed from the simulated TEM images with zone axes of (**B** and **F**) [100] and (**C** and **G**) [110]. The reconstruction maps are obtained with a parameter of 1,000 projection directions. (**D** and **H**) Distributions of atomic position deviations, showing a root mean square deviations of (**D**) 2.6 pm and (**H**) 5.6 pm. (**A** to **D**) 2.5 nm-sized Pt nanocrystal and (**E** to **H**) 4.0 nm-sized Pt nanocrystal. Scale bars, 1 nm.


**Fig. S12.**
Comparison between (top) original TEM images, (middle) reprojected images (simple sum), and (bottom) multi-slice simulated images from the eight Pt nanocrystals. (**A** to **F**) single crystalline particles, (**G**) particle with distorted crystal, (**H**) particle with dislocation.

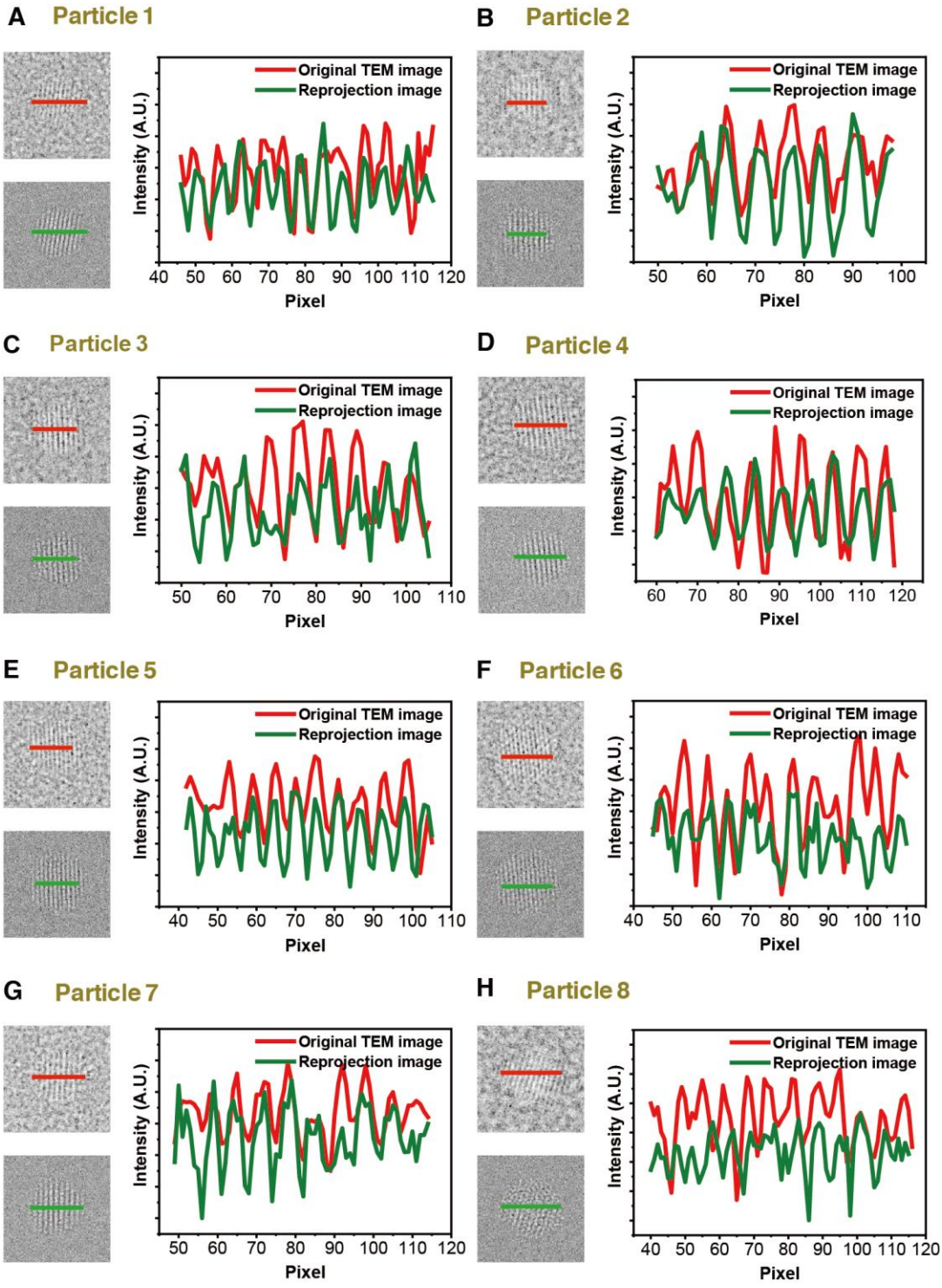


**Fig. S13.**
Intensity profiles of representative raw TEM images and simulated images by multi-slice simulation of the eight Pt nanocrystals. (**A** to **F**) single crystalline particles, (**G**) particle with distorted crystal, (**H**) particle with dislocation.

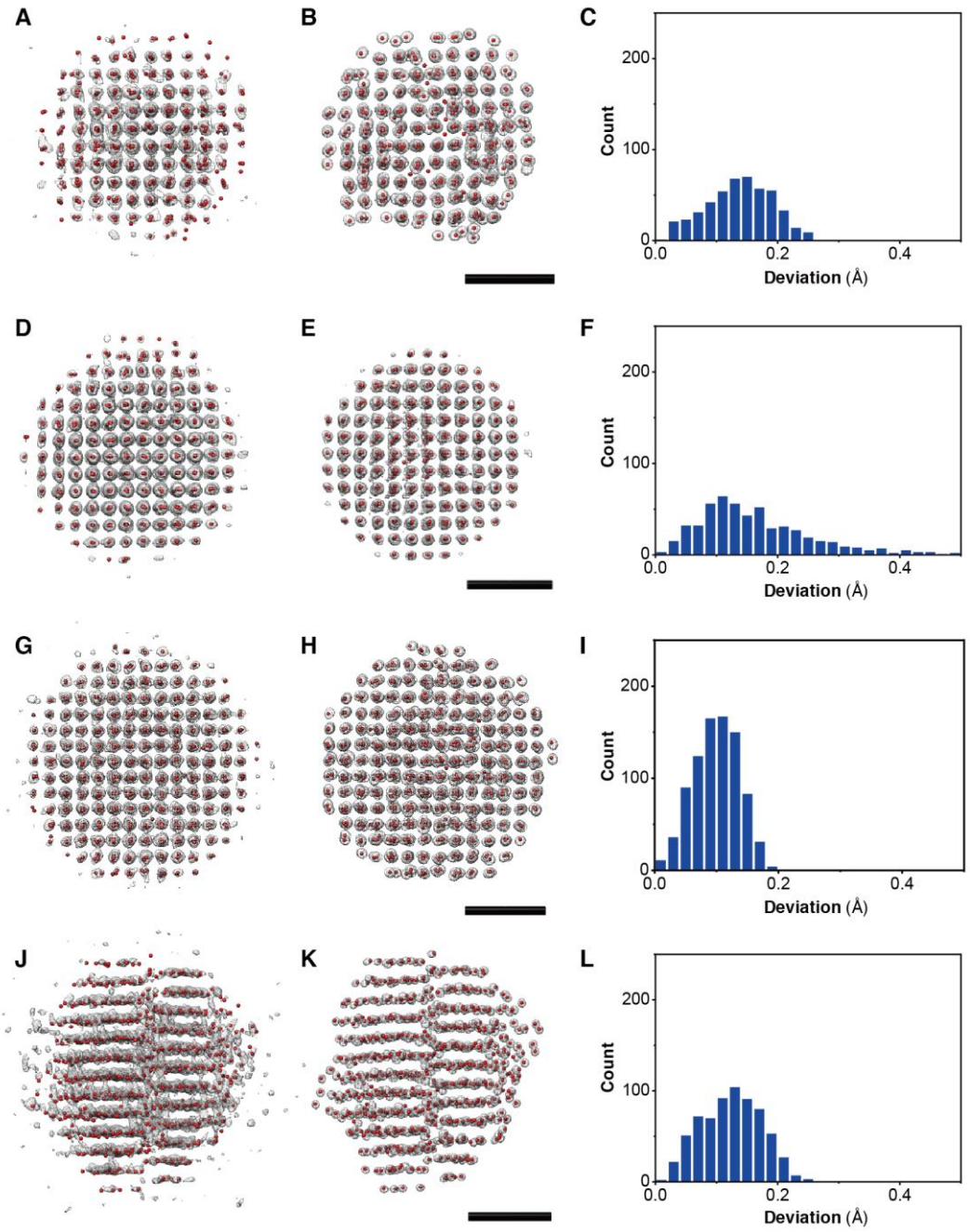


**Fig. S14.**

(**A**, **D**, **G**, and **J**) 3D density maps overlaid with atomic coordinates of Pt nanocrystals reconstructed from the original TEM images. (**B**, **E**, **H**, and **K**) Re-reconstructed 3D density map overlaid with atomic coordinates of nanocrystals reconstructed from the simulated TEM images of the reconstructed atomic map. (**C**, **F**, **I**, and **L**) Distribution of atomic position deviation. (**A** to **C**) Particle 2, showing a root mean square deviation of 14 pm. (**D** to **F**) Particle 4, showing a root mean square deviation of 19 pm. (**G** to **I**) Particle 6, showing a root mean square deviation of 9.9 pm. (**J** to **K**) Particle 8, showing a root mean square deviation of 12 pm. Scale bars, 1 nm.

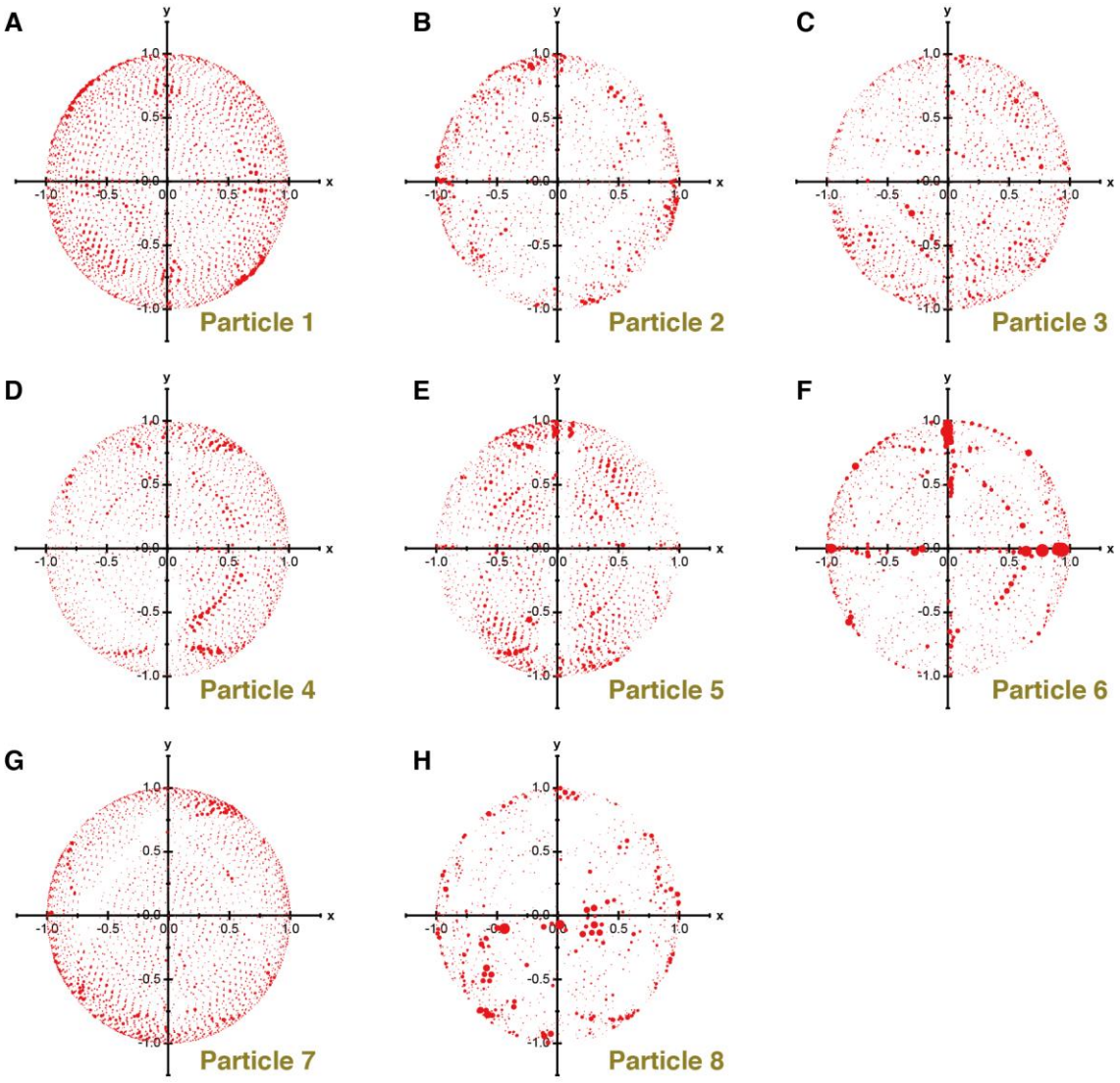


**Fig. S15.**
Orientation coverage allocated onto *xy*- planes. Orientation coverage plots of (**A** to **F**) Single crystalline particles, (**G**) particle with distorted crystal, and (**H**) particle with dislocation.

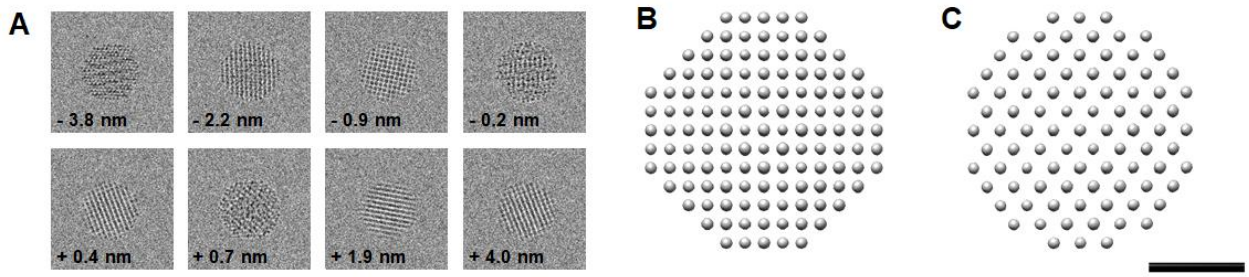


**Fig. S16.**

(**A**) Simulated TEM images obtained from multi-slice simulation of a model Pt nanocrystal with a size of 2.5 nm that has defocus following a Gaussian distribution within a range of 10 nm and standard deviation of 1.7 nm. (**B, C**) 3D density maps reconstructed from the multi-slice simulated images in a viewing direction of (**B**) [100] and (**C**) [110].

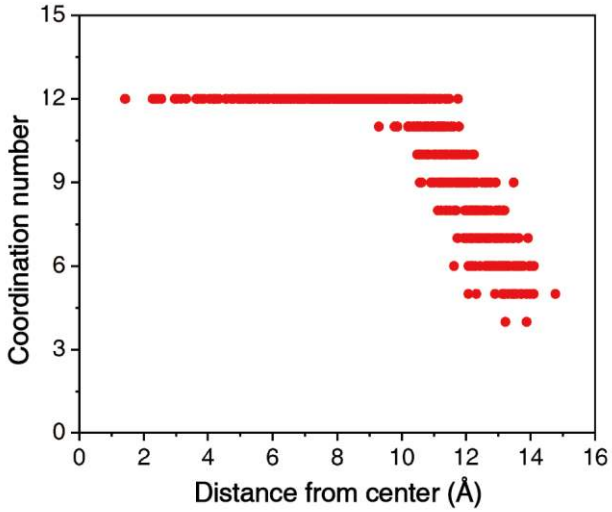


**Fig. S17.**
Depth profile of coordination numbers in reconstructed Particle 4.

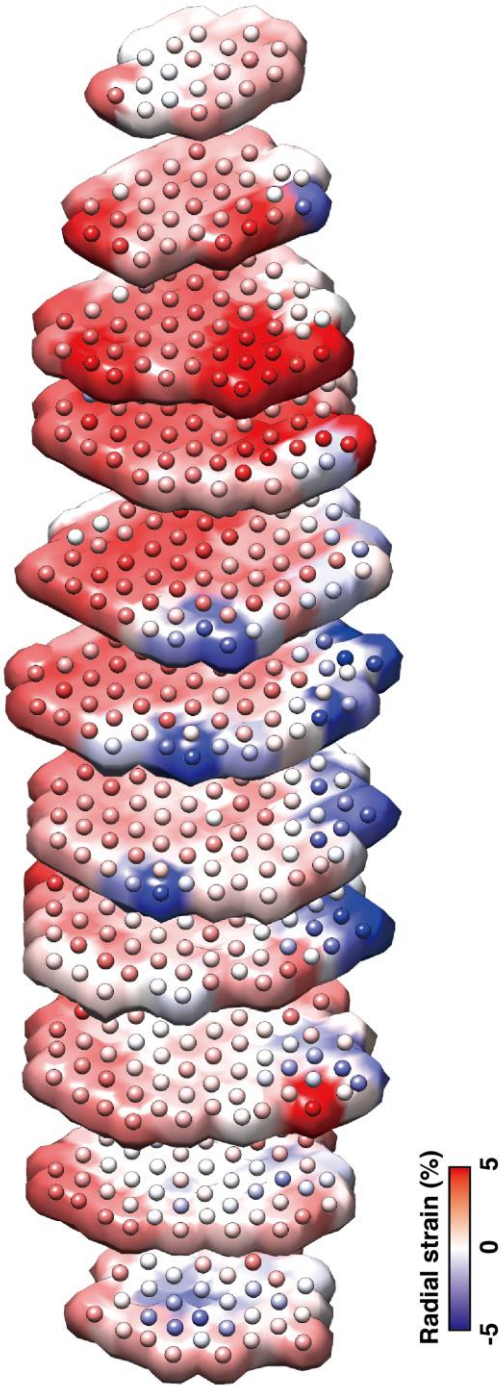


**Fig. S18.**
Sliced images of the radial strain map ($\varepsilon_{rr}$) of Particle 4. Strain is indicated by color gradient from red (5%), white (0%) to blue (-5%) colors.

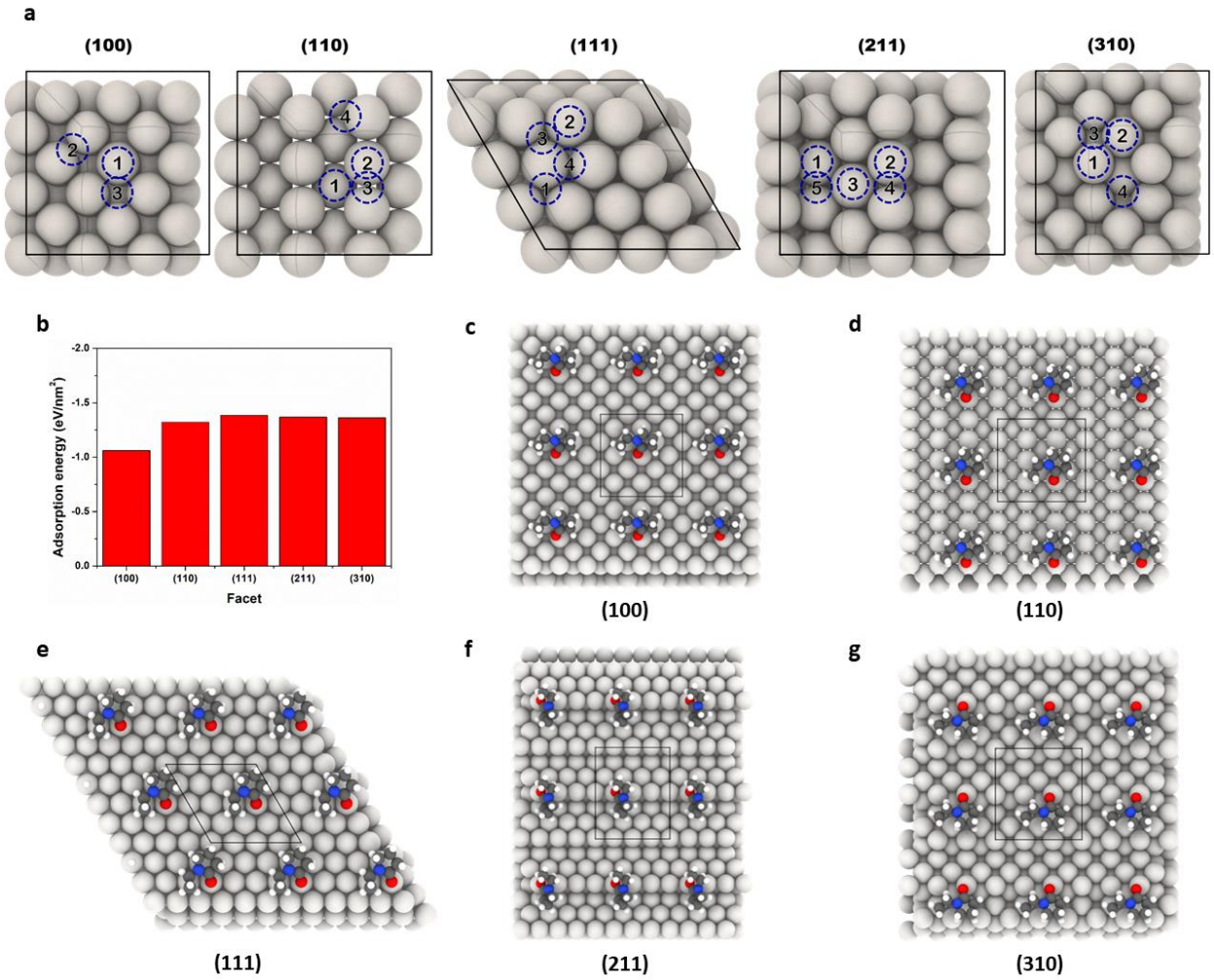


**Fig. S19.**
(A) Calculated adsorption sites and (**B**) adsorption energy of binding units of PVP ligand on different facets of Pt. Five facets typically appearing in reconstructed Pt nanocrystals were selected. Pictures for C to F show optimized geometries for a single unit of a PVP ligand in the Pt surfaces: (**C**) (100), (**D**) (110), (**E**) (111), (**F**) (211), and (**G**) (310) facets.

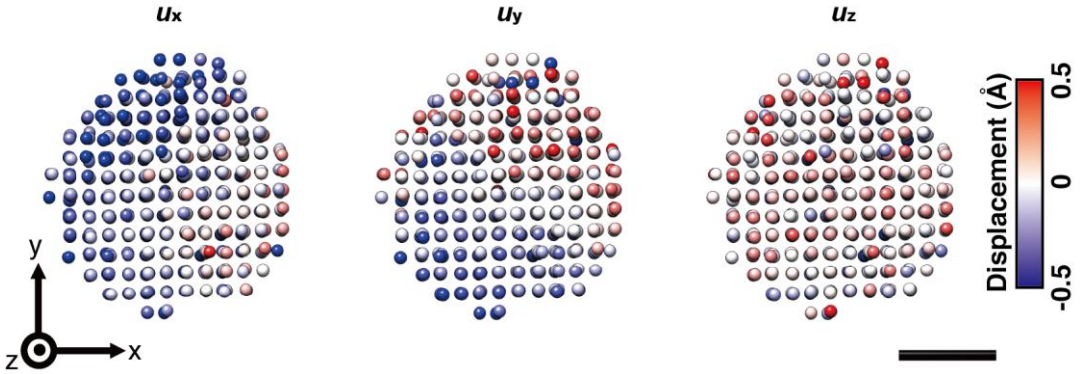


**Fig. S20.**
Displacement fields for each atomic position of Particle 4. Displacement is indicated by color gradient from red (0.5 Å), white (0 Å) to blue (-0.5 Å) colors. Scale bar, 1 nm.

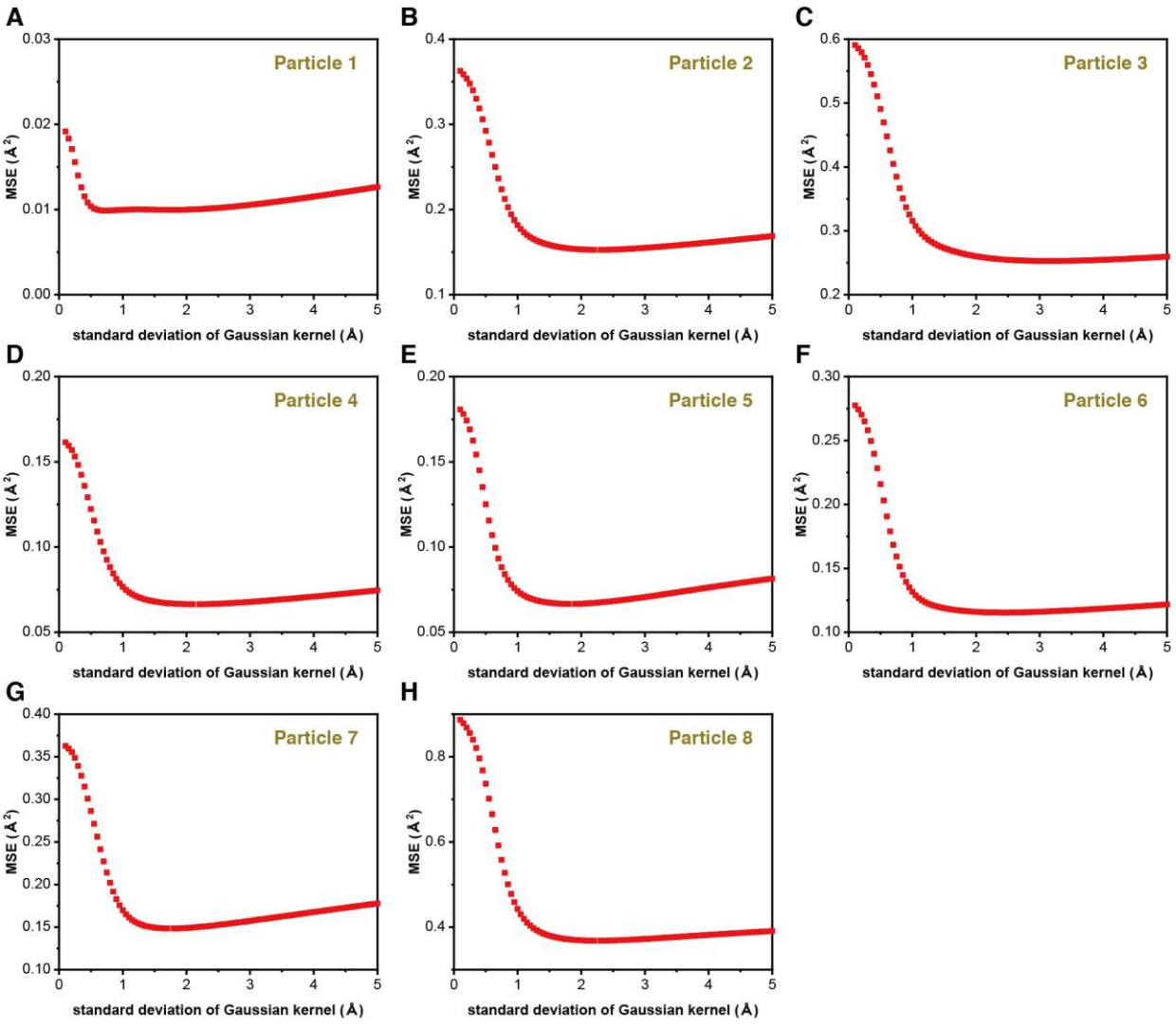


**Fig. S21.**
The results of leave-one-out cross-validation (LOOCV). Mean square error (MSE) curve versus standard deviation of Gaussian kernel for the eight reconstructed Pt nanocrystals. (**A** to **F**) single crystalline particles, (**G**) particle with distorted crystal, (**H**) particle with dislocation.

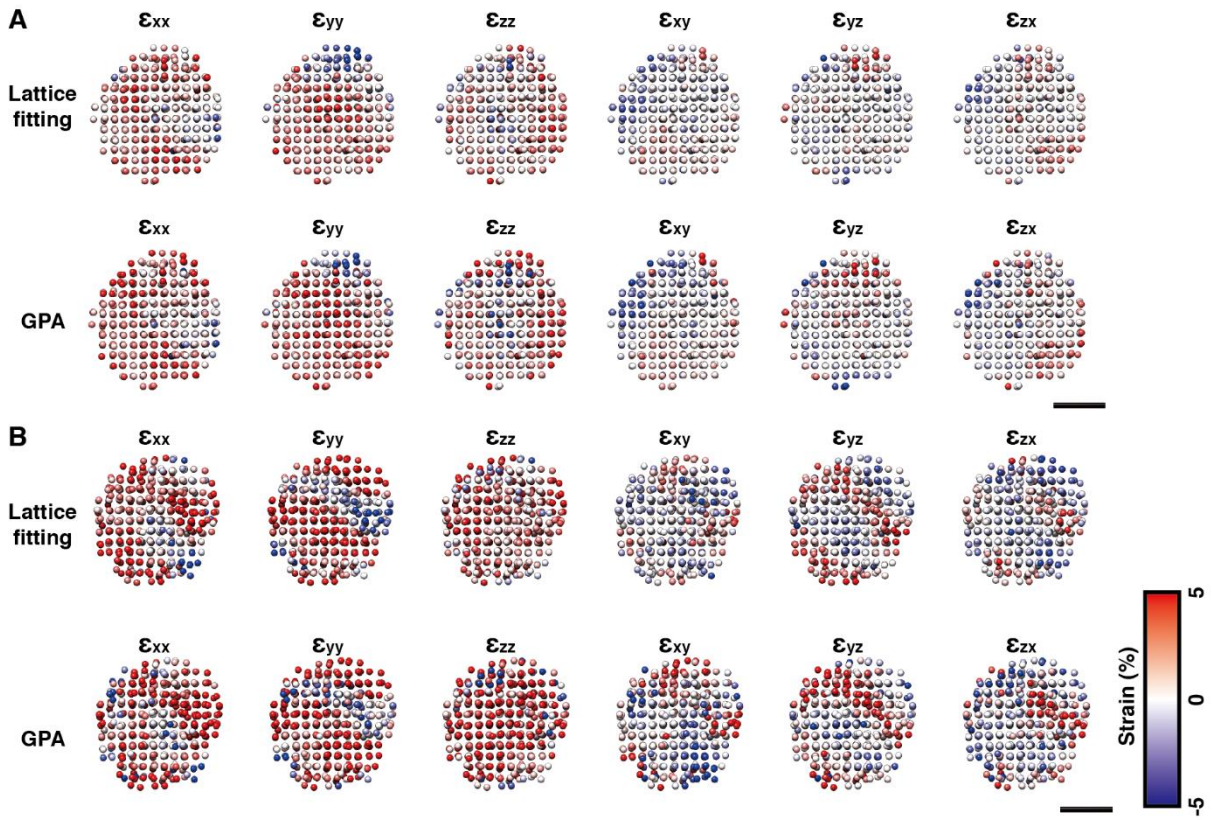


**Fig. S22.**
Six components of strain tensors of (**A**) the single crystalline particle (Particle 4) and (**B**) distorted particle (Particle 7). Strain maps in top panels were obtained by differentiating displacement fields after lattice fitting while the maps in bottom panels were obtained by GPA method. Strain is indicated by color gradient from red (5%), white (0%) to blue (-5%) colors. Scale bars, 1 nm.

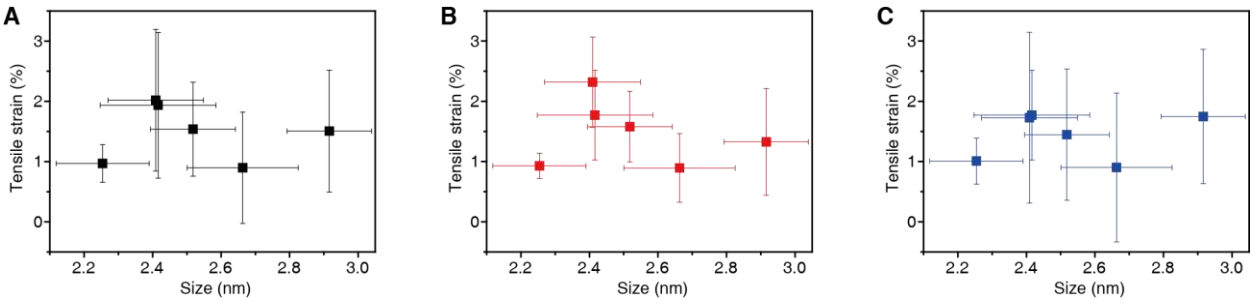


**Fig. S23.**
Correlation between size and tensile strains of single crystalline nanocrystals (Particle 1 to 6). (**A**) Strains of all constituent atoms, (**B**) strains of core atoms, and (**C**) strains of surface atoms. The surface atoms are defined by the following equation, $r > R - d_{111}$, where $r$ is an atomic position from center of mass, $R$ is the radius of the nanocrystal, and $d_{111}$ is the bulk Pt(111) plane distance.

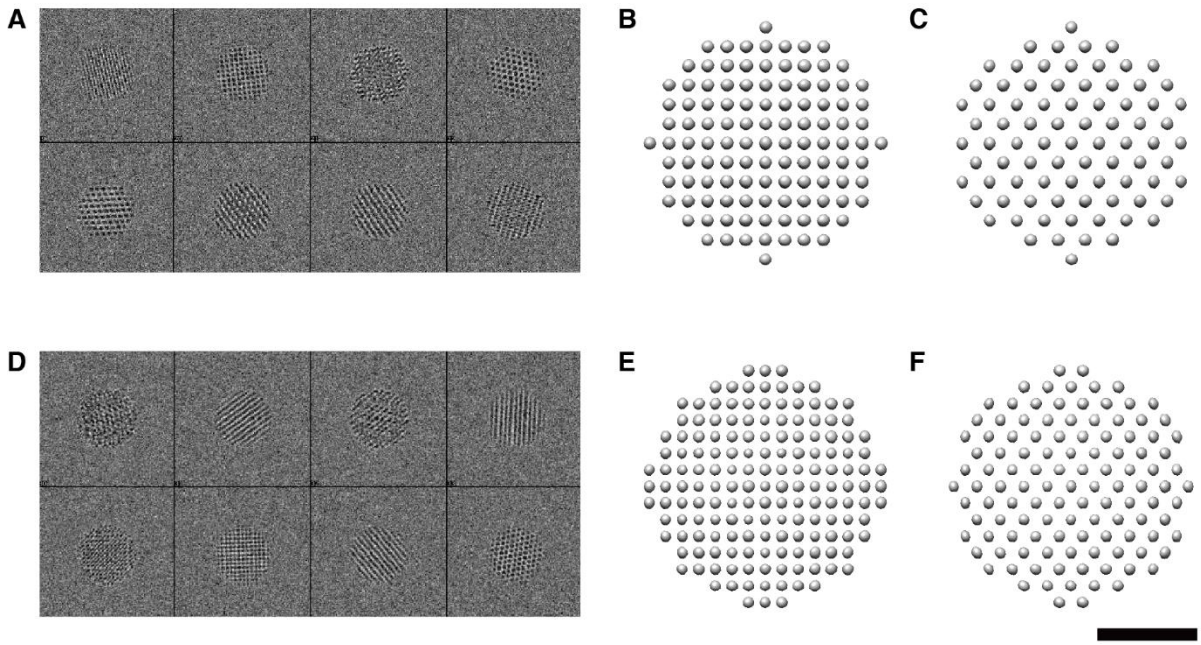


**Fig. S24.**

(**A** and **D**) Simulated TEM images obtained from multi-slice simulation of (**A**) a model 2.5 nm-sized spherical Ag nanocrystal with bulk fcc structure and (**D**) a model 2.5 nm-sized spherical Ni nanocrystal with bulk fcc structure. Noises were added with a signal-to-noise ratio of 0.2. (**B**, **C**, **E**, and **F**) 3D volume maps reconstructed from the multi-slice simulated images of (**B** and **C**) the model Ag nanocrystals and (**E** and **F**) the model Ni nanocrystals. The viewing directions are (**B** and **E**) [100] and (**C** and **F**) [110]. The reconstruction maps are obtained with a parameter of 1,000 projection directions. Scale bar, 1 nm.

| | Type | Size (nm) | Number of atoms | Lattice parameter (Å) | Formation energy (eV/atom) |
|---|---|---|---|---|---|
| Particle 1 | Single crystal | 2.25 | 398 | 3.960 | 0.706 |
| Particle 2 | Single crystal | 2.41 | 486 | 4.020 | 1.213 |
| Particle 3 | Single crystal | 2.42 | 489 | 3.999 | 0.980 |
| Particle 4 | Single crystal | 2.52 | 555 | 3.988 | 0.366 |
| Particle 5 | Single crystal | 2.66 | 655 | 3.957 | 0.407 |
| Particle 6 | Single crystal | 2.92 | 863 | 3.968 | 0.706 |
| Particle 7 | Distorted | 2.44 | 504 | 4.021 | 0.897 |
| Particle 8 | Dislocation | 2.69 | 674 | 3.859 | 2.579 |

**Table S1.**
Size, lattice parameter, and energy of the eight reconstructed Pt nanocrystals.

| Facet | Adsorption site | Adsorption energy (eV/nm$^2$) |
|---|---|---|
| (100) | 1 | -1.208 |
| | 2 | -1.061 |
| | 3 | -0.932 |
| (110) | 1 | -1.322 |
| | 2 | -1.318 |
| | 3 | -1.308 |
| | 4 | -1.288 |
| (111) | 1 | -1.383 |
| | 2 | -1.322 |
| | 3 | -1.319 |
| | 4 | -1.306 |
| (211) | 1 | -1.368 |
| | 2 | -1.015 |
| | 3 | -0.809 |
| | 4 | -0.785 |
| | 5 | -0.731 |
| (310) | 1 | -1.361 |
| | 2 | -1.183 |
| | 3 | -0.963 |
| | 4 | -0.796 |

**Table S2.**
Adsorption energies of PVP on Pt surfaces with different adsorption sites.

**Captions for movies**

**Movie S1.**
Cropped movie of (left) raw TEM images and (right) weighted averaged TEM image of Particle 1. The movie contains 2,800 sequential images after tracking and cropping.

**Movie S2.**
3D density maps, atomic position maps, and strain maps of 8 reconstructed nanocrystals.